Stem Cell Reports
Article

ISSCR

OPEN ACCESS

CRISPR/Cas9/AAV9-mediated *in vivo* editing identifies MYC regulation of 3D genome in skeletal muscle stem cell

Liangqiang He,[1,4] Yingzhe Ding,[1,4] Yu Zhao,[2,3,4] Karl K. So,[1] Xianlu L. Peng,[1] Yuying Li,[2] Jie Yuan,[1] Zhiming He,[1] Xiaona Chen,[2] Hao Sun,[1,*] and Huating Wang[2,*]

[1]Department of Chemical Pathology, Li Ka Shing Institute of Health Sciences, The Chinese University of Hong Kong, Hong Kong, China
[2]Department of Orthopaedics and Traumatology, Li Ka Shing Institute of Health Sciences, The Chinese University of Hong Kong, Hong Kong, China
[3]Present address: Molecular Cancer Research Center, School of Medicine, Sun Yat-sen University, Shenzhen, China
[4]These author contributed equally
*Correspondence: haosun@cuhk.edu.hk (H.S.), huating.wang@cuhk.edu.hk (H.W.)
https://doi.org/10.1016/j.stemcr.2021.08.011

SUMMARY

Skeletal muscle satellite cells (SCs) are stem cells responsible for muscle development and regeneration. Although CRISPR/Cas9 has been widely used, its application in endogenous SCs remains elusive. Here, we generate mice expressing Cas9 in SCs and achieve robust editing in juvenile SCs at the postnatal stage through AAV9-mediated short guide RNA (sgRNA) delivery. Additionally, we reveal that quiescent SCs are resistant to CRISPR/Cas9-mediated editing. As a proof of concept, we demonstrate efficient editing of master transcription factor (TF) *Myod1* locus using the CRISPR/Cas9/AAV9-sgRNA system in juvenile SCs. Application on two key TFs, MYC and BCL6, unveils distinct functions in SC activation and muscle regeneration. Particularly, we reveal that MYC orchestrates SC activation through regulating 3D genome architecture. Its depletion results in strengthening of the topologically associating domain boundaries thus may affect gene expression. Altogether, our study establishes a platform for editing endogenous SCs that can be harnessed to elucidate the functionality of key regulators governing SC activities.

INTRODUCTION

Skeletal muscle is built up by numerous multinucleated myofibers and presents excellent regeneration potential after injury, which is executed by adult muscle stem cells also called satellite cells (SCs) (Ancel et al., 2021). Normally, juvenile SCs characterized by paired-box gene 7 (PAX7) expression emerge about 2 days before birth in mice and continue to proliferate to form adult muscle through undergoing postnatal myogenesis. About 2–4 weeks after birth, quiescent SCs (QSCs) appear to build the SC pool (Tajbakhsh, 2009). In healthy adult skeletal muscle, PAX7+ QSCs are located in a specialized niche beneath the basal lamina. Upon traumas, these dormant SCs quickly activate and re-enter the cell cycle to give rise to myoblasts characterized by elevated expression of two basic helix-loop-helix (bHLH) transcription factors (TFs), myogenic factor 5 (MYF5) and MYOD1. Then a large portion of myoblasts downregulate PAX7 expression and undergo myogenic differentiation to form new muscle fibers by inducing MYOGENIN and myogenic regulatory factor 4 (MRF4) expression. Meanwhile, a sub-population of activated SCs retaining high PAX7 expression return to quiescence to restore the SC pool (Ancel et al., 2021).

Transcriptional regulation orchestrated by TFs represents the key intrinsic mechanism driving SC fate transition and lineage progression (Ancel et al., 2021). However, a systematic approach is needed to identify potential key TFs modulating SC quiescence and early activation. Moreover, an effective approach is needed to test the functionality of the above predicted key TFs. In particular, since quiescence cannot be maintained once the cells are isolated (Machado et al., 2017), TFs that function in QSCs thus need to be manipulated *in vivo*, which calls for an effective *in vivo* genome editing system.

Recently, the *in vivo* application of CRISPR/Cas9 is emerging to generate mouse models and to correct genetic diseases by viral or non-viral based Cas9/short guide RNA (sgRNA) delivery (Doetschman and Georgieva, 2017). In particular, several reports described its utility in skeletal muscle tissue (Doetschman and Georgieva, 2017; Tabebordbar et al., 2016) treating Duchenne muscular dystrophy (DMD). In these attempts, co-transduction of multiple adeno-associated virus (AAV) vectors is required to deliver the Cas9 and sgRNAs separately considering the restricted packaging capacity of AAV virus (~4.7 kb), which, however, limited the modification efficiency since successful editing only occurs in nuclei simultaneously receiving all the components. In addition, as most of the genomic modifications were conducted in post-mitotic myofibers, it remains to be determined whether such AAV/Cas9/sgRNA-based tools can be applied to edit SCs *in vivo*. Moreover, muscle-related studies would tremendously benefit from a facile *in vivo* platform which allows disruption of gene expression in endogenous SCs instead of isolating them or generating multiallelic transgenic mice (Goldstein et al., 2019). However, several issues need to be clarified before the generation of such a tool. The most conflicting one is whether AAV vectors are able to transduce SCs *in vivo*. While a previous study concluded that QSCs are resistant to AAV

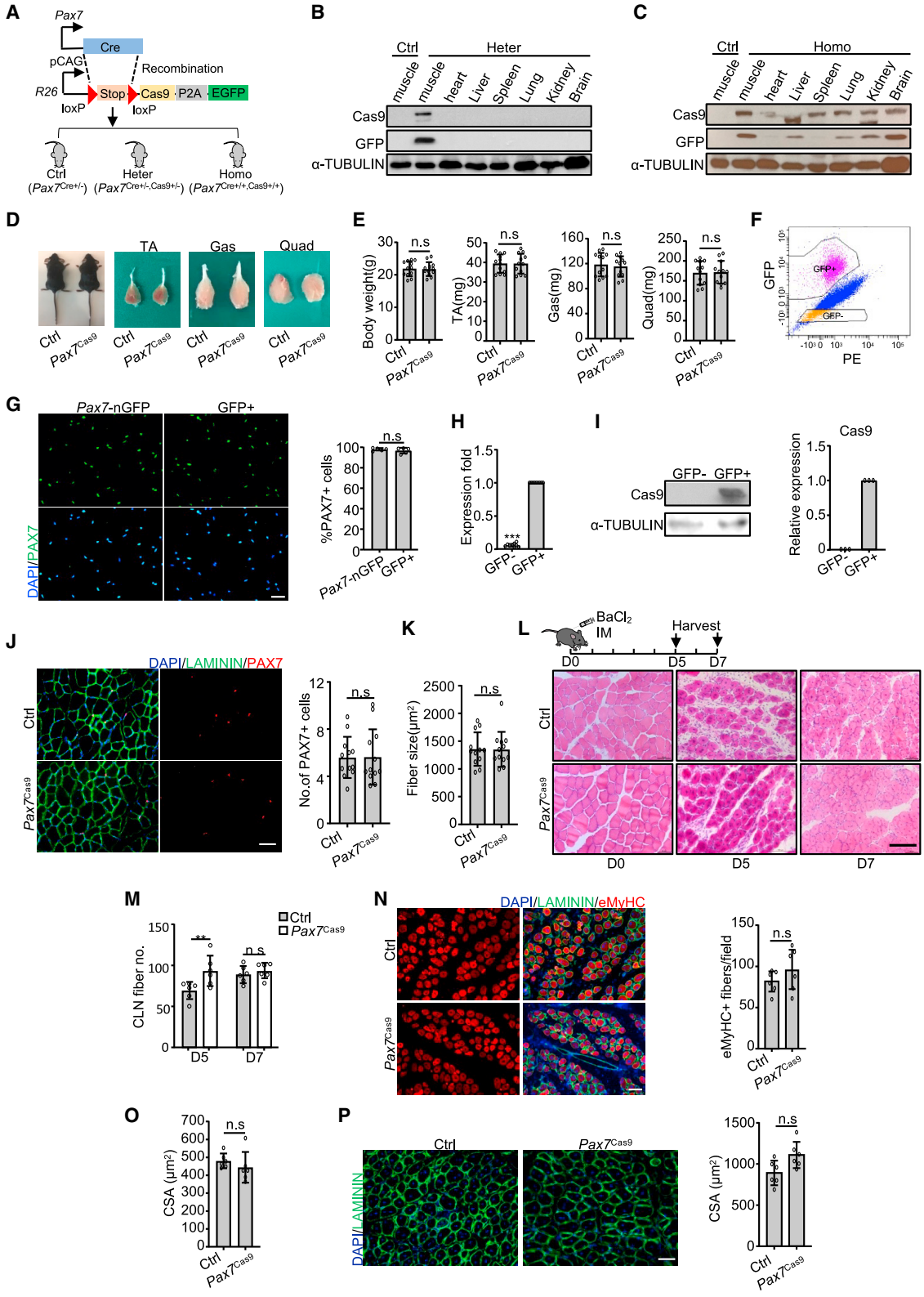

(legend on next page)

transduction (Arnett et al., 2014), two recent studies reported efficient transduction of multiple AAV serotypes to SCs in adult mice by a Cre/lox fluorescent reporter tracking system (Goldstein et al., 2019; Nance et al., 2019). Even with efficient transduction, the ability of CRISPR/Cas9 to modify genomes in endogenous SCs still needs to be tested. To this end, one study demonstrated successful editing in proliferating juvenile SCs with modest efficiency (2%–4% of endogenous SCs were edited) by injecting the AAV virus at postnatal stage (Tabebordbar et al., 2016), and another recent study found weak genome modification of CRISPR/Cas9 in adult mice by using a muscle graft model (Nance et al., 2019). Since both of the editing events occurred during active myogenesis, these findings hint that CRISPR/Cas9 may be able to modify SCs in certain settings. Nevertheless, whether QSCs in the adult stage are permissive to CRISPR/Cas9-mediated genome editing is still unknown.

Here, in this study, we generate a mouse line expressing Cas9 in SCs to evaluate the feasibility of CRISPR/Cas9-based genome modification in endogenous SCs. Cas9 expression in SCs does not have obvious impact on SC homeostasis and regenerative capacity. Robust editing by CRISPR/Cas9 was observed in juvenile SCs undergoing active myogenesis; up to 95% editing efficiency was achieved on the *Myod1* locus, which resulted in a complete depletion of MYOD1 protein. Using this *in vivo* editing system, we tested the functionality of two potential key TFs, MYC and BCL6, and uncovered their distinctive importance in SC activation and muscle regeneration. Furthermore, we found that MYC promotes SC activation through remodeling 3D genome architecture. Interestingly, application of the above system in adult SCs at quiescent stage did not yield successful editing even with efficient AAV9 transduction. Altogether, our study thus establishes a CRISPR/Cas9/AAV9-sgRNA genome editing system in endogenous SCs, which can be harnessed to identify and elucidate the functions of key TFs or other regulators orchestrating SC activities.

RESULTS

Prolonged expression of Cas9 protein has no obvious impact on SC function

To demonstrate the feasibility of harnessing CRISPR/Cas9 to modify the genome in endogenous SCs, we first generated a mouse line that expressed Cas9 in SCs. We crossed Cre-dependent *Rosa26*$^{Cas9-EGFP}$ knockin mouse (Platt et al., 2014) with a *Pax7*^{Cre} knockin mouse to generate heterozygous (*Pax7*$^{Cre+/-,\ Cas9+/-}$) and homozygous (*Pax7*$^{Cre+/+,\ Cas9+/+}$) mice along with the control (Ctrl) (*Pax7*$^{Cre+/-}$) (Figure 1A). Co-expression of GFP facilitated us to monitor the Cas9-expressing cells. Cas9 and GFP proteins were restrictively expressed in muscle but not in other tissues of heterogeneous mice or muscle tissue of Ctrl mice (Figure 1B). PAX7 is known to be expressed in brain, especially in the hypothalamus (Hosoyama et al., 2010); the absence of detected expression in brain tissue is probably because only a small part, not the whole brain, was collected for detection. However, in some homozygous mice, Cas9 was expressed in multiple tissues (Figure 1C), possibly because PAX7 was expressed in a rare sub-population of spermatogonia of mice and thus turned on Cas9 expression as early as in the zygote (Aloisio et al., 2014). Therefore, the heterogeneous mice were used for the following experiments and referred to as *Pax7*^{Cas9} mice. The *Pax7*^{Cas9} progenies showed no overt morphological

Figure 1. Prolonged expression of Cas9 protein has no obvious impact on SC function

(A) Generation of mice expressing Cas9 in SCs. KI, knock in.

(B and C) Cas9 and GFP expressions were examined in heterozygous (B) and some homozygous mice (C).

(D and E) No obvious difference was detected between Ctrl and *Pax7*^{Cas9} littermates (TA, tibialis anterior; Gas, gastrocnemius; Quad, quadriceps). Representative images (D) and quantification (E) are shown. n = 12 mice.

(F) The gating strategy to isolate Cas9-GFP positive SCs. The phycoerythrin (PE) channel (biexponential scale) was used to separate GFP+ and GFP− cells.

(G) Left: IF staining of PAX7. n = 5 mice (an average of six fields/mouse). Scale bar, 50 μm.

(H) Cas9 mRNAs were detected (normalized to *18S* mRNA). n = 9 independent experiments.

(I) Cas9 expression was examined and the band intensity was quantified. n = 3 independent experiments.

(J) Left: immunostaining of PAX7 and LAMININ on the TA muscle from 8-week-old mice. Right: the number of PAX7+ cells per 100 fibers. n = 12 mice (an average of six fields/mouse). Scale bar, 50 μm.

(K) Average fiber size. n = 12 mice.

(L and M) H&E staining on day 5 and 7 post injury (L). Myofibers with CLN per field (M). n = 6 mice (an average of five fields/mouse). Scale bar, 100 μm.

(N) Left: immunostaining of eMyHC and LAMININ at day 5 post injury. Right: the number of eMyHC+ myofibers. n = 6 mice (an average of six fields/mouse). Scale bar, 50 μm.

(O) CSA of the fibers with CLN at day 5 post injury. n = 6 mice.

(P) Left: immunostaining of LAMININ at day 7 post injury. Right: CSA of the fibers with CLN. n = 6 mice (an average of three fields/mouse). All the bar graphs are presented as mean ± SD. **p < 0.01. ns, no significance.

abnormalities (Figures 1D and 1E). To confirm the expression of Cas9 protein, SCs were isolated by fluorescence-activated cell sorting (FACS). Two distinguishable sub-populations appeared on the sorting plot based on GFP signals (Figure 1F) and up to 97% of GFP+ cells also expressed PAX7 (Figure 1G); the purity was similar to that of SCs isolated from *Pax7*-nGFP mice (96.74% ± 2.81% versus 97.85% ± 1.4%) (Figure 1G). High expression of Cas9 mRNA and protein were detected in GFP+ SCs but not in GFP− cells (Figures 1H and 1I). Furthermore, the number of PAX7+ SCs was not affected by prolonged Cas9 expression (Figure 1J) and the average fiber size showed no difference compared with the Ctrl mice (Figure 1K). To further investigate the effect of ectopic expression of Cas9 on SC function, acute muscle injury was induced by injection of barium chloride ($BaCl_2$) into the tibialis anterior (TA) muscles (Figures 1L). Although more regenerating myofibers with centrally localized nuclei (CLN) were detected in $Pax7^{Cas9}$ versus Ctrl at 5 days post injury, the difference disappeared at day 7 (Figures 1L and 1M). Immunostaining of eMyHC, a marker of newly formed fibers that may not have formed CLNs, on the other hand, revealed that the number of eMyHC+ fibers was comparable at 5 days after injury (Figure 1N). Moreover, the cross-sectional areas (CSA) of the newly formed fibers at days 5 and 7 revealed no obvious difference (Figures 1O and 1P). Altogether, the above results demonstrate that Cas9 expression in SCs does not cause obvious impact on SC homeostasis and regenerative capacity.

CRISPR/Cas9 in conjunction with AAV9-mediated sgRNAs delivery yields robust editing in juvenile SCs

Next, we sought to test whether SCs can be efficiently edited *in vivo* using the above $Pax7^{Cas9}$ mouse. To this end, we first tested whether this is feasible using juvenile SCs since a previous study reported mild editing efficiency in SCs at postnatal stage (Tabebordbar et al., 2016). As a proof of concept, the *Myod1* gene was selected due to the wealth of knowledge of its function in SCs as a master TF orchestrating myogenic program (Peng et al., 2017; Yamamoto et al., 2018). A total of six sgRNAs against the first coding exon of *Myod1* were designed (Figure 2A) and each was cloned into a Cas9-GFP-expressing vector and transfected into C2C12 cells followed by FACS to enrich transfected cells (Figure S1A); sgRNA2 showing the highest editing efficiency (19.5%) by Surveyor nuclease assay was chosen for further use. To deliver the sgRNA *in vivo*, sgRNA2 was placed into a U6-driven pAAV9-sgRNA vector (Figure 2A), which also carries a fluorescent dsRed gene; this AAV9-sgMyod1 resulted in an obvious cleavage at *Myod1* locus (28.3%) *in vitro* (Figure S1B).

The above AAV9-sgMyod1 plasmid was then packed into virus particles and intramuscularly (IM) injected into the $Pax7^{Cas9}$ mice with a single dose of 2×10^{11} viral genomes (vg)/mouse at postnatal day 10 (P10) (Figure S1C). At this stage of postnatal myogenesis, it is known that myogenic precursor cells actively proliferate to increase adult muscle; upon the termination of the postnatal myogenesis around P21 (Tajbakhsh, 2009), a portion of the edited myoblasts are expected to become quiescence SCs carrying the editing event (Figure S1D). For the Ctrl group, the same dose of AAV9 virus containing pAAV9-sgRNA backbone without any sgRNA insertion was injected. Four weeks after injection, we first evaluated the transduction efficiency of AAV9 virus into SCs. As expected, two distinguishable sub-populations were separated on the plot according to GFP expression (Figure S1E); intriguingly, the GFP+ SCs did not present differential dsRed expression. However, further examination of dsRed signal in the input cells (Figure S1E) by histogram showed there was indeed a separation of dsRed-high versus -low populations and GFP+ cells were located in the dsRed-high peak (Figure S1F), indicating that most GFP-expressing SCs were indeed infected by the virus. Moreover, immunofluorescence (IF) staining showed above 80% of the isolated SCs (GFP+) were dsRed positive (Figures S1G and S1H). These findings indicated that the above-administered AAV9 dosage was high enough to infect all the GFP+ SCs, thus the GFP+ population was isolated for following analyses. To estimate the editing efficiency, genomic DNAs from freshly isolated SCs (FISCs) were subject to Surveyor assay; around 30%–40% indel occurrence at the targeted *Myod1* locus was detected in the AAV9-sgMyod1-injected mice but not in the Ctrl group (Figure S1I). Further Surveyor analysis of *Myod1* transcripts from SCs cultured for 4 days also verified efficient mutagenesis (Figure S1J). Taken together, the above results demonstrate the juvenile SCs at postnatal stage can be efficiently edited in $Pax7^{Cas9}$ mice.

A recent study implied that the administration of high-dose AAV9 virus particles to non-human primates and piglets caused severe toxicity (Hinderer et al., 2018), so we sought to determine the minimal dose of AAV9 needed to achieve effective editing. To this end, high (5×10^{11} vg/mouse), middle (1×10^{11} vg/mouse), or low (0.2×10^{11} vg/mouse) doses of AAV9-sgMyod1 virus particles were intramuscularly injected into $Pax7^{Cas9}$ mice at P10 (Figure 2B) with no obvious abnormalities observed even in the high-dose group. Four weeks after injection, a slightly higher editing efficiency in the middle- versus low-dose group was observed, but no obvious difference between the middle- and high-dose groups (Figures S2A and S2B). To precisely determine the level of editing, sgMyod1 targeted locus was amplified from genomic DNAs in FISCs and subject to deep sequencing. The high-dose treatment led to a significantly higher level of mutations than the low- (95.08% ± 0.80% versus 83.16% ± 1.42%) or

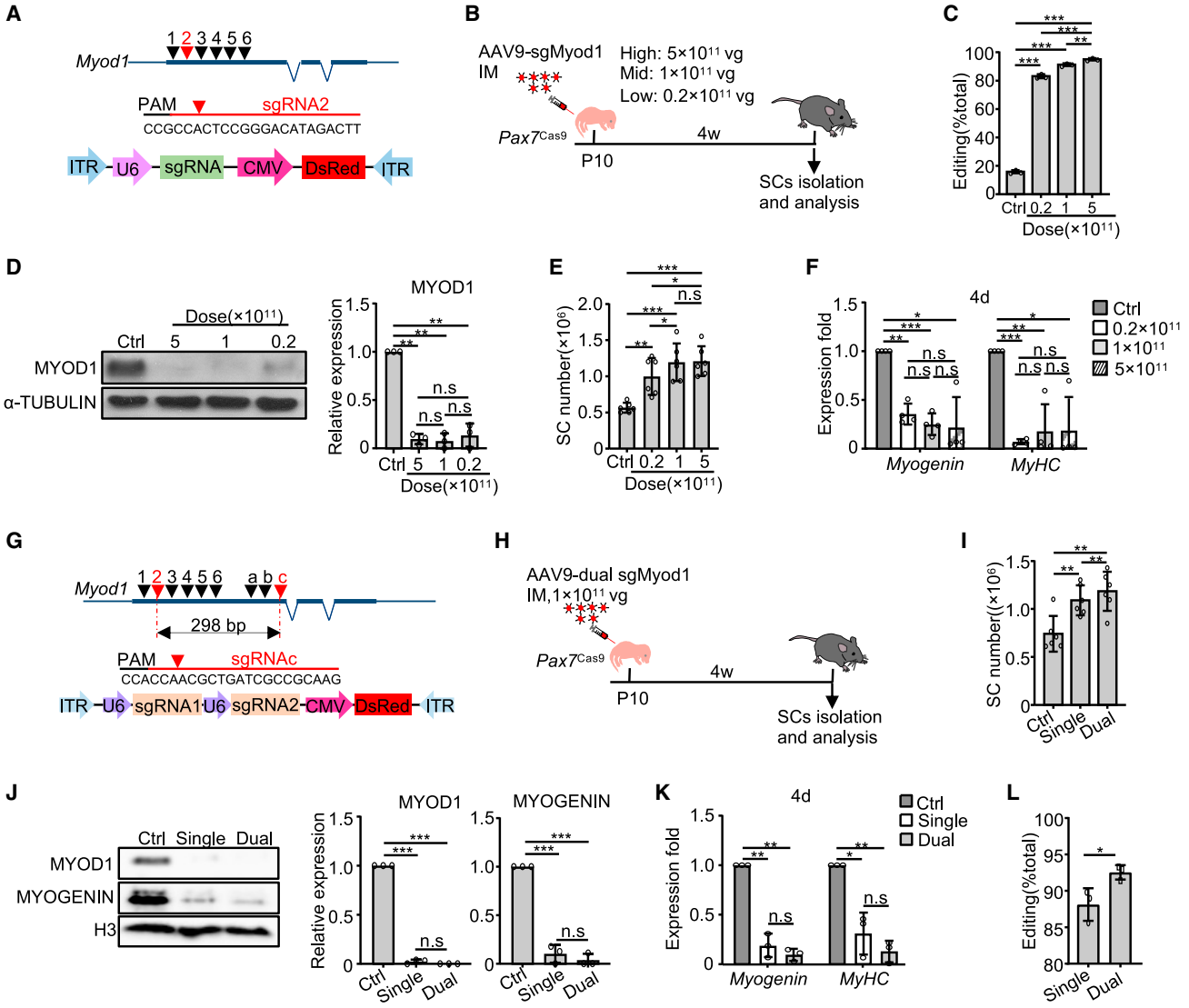

Figure 2. CRISPR/Cas9 in conjunction with AAV9-mediated sgRNAs delivery yields robust editing in juvenile SCs

(A) Top: sgRNAs for targeting the *Myod1* locus. Middle: selected sgRNA2 and its targeted sequence. Bottom: illustration of the vector. PAM, protospacer-adjacent motif.

(B) Illustration of the experimental design.

(C) Quantification of the editing efficiency (calculated as the ratio of the edited reads to the total reads). n = 3 mice.

(D) SCs were cultured for 2 days and the MYOD1 protein level was examined (left); the band intensity was quantified by ImageJ (right). n = 3 mice.

(E) The number of purified SCs. n = 6 mice.

(F) SCs were cultured for 4 days and the *Myogenin* or *MyHC* mRNAs were detected. n = 4 mice.

(G) Top: dual sgRNAs targeting *Myod1*. Middle: the targeted sequence for sgRNAc. Bottom: illustration of the vector.

(H) Illustration of the experimental design.

(I) The number of sorted FISCs. n = 6 mice.

(J) SCs were cultured for 2 days and the protein levels of MYOD1 and MYOGENIN were examined (left); the band intensity was quantified (middle and right). n = 3 mice.

(K) *Myogenin* and *MyHC* mRNAs in SCs cultured for 4 days. n = 3 mice.

(L) Quantification of the editing efficiency. n = 3 mice. All qRT-PCR data were normalized to *18S* or *Gapdh* mRNA. All the bar graphs are presented as mean ± SD. *p < 0.05, **p < 0.01, and ***p < 0.001. ns, no significance.

See also Figures S1 and S2.

middle-dose groups (91.28% ± 0.92%) (Figure 2C); however, the percentage of frameshift mutations between the high- and middle-dose groups showed no obvious difference (77.43% ± 1.42% versus 75.58% ± 2.26%) (Figures S2C and S2D). A >80% indel formation frequency (Figure 2C) further confirmed that the AAV9 virus efficiently transduced SCs and the copy number of sgRNAs was high enough to achieve efficient editing even in the low-dose group.

At the protein level, we found that MYOD1 protein was completely eliminated in SCs from the high- or middle-dose groups, whereas a noticeable expression in the low-dose group was present (Figures 2D and S2E). However, we failed to observe a sharp decrease in *Myod1* transcript levels (Figure S2F), suggesting that CRISPR/Cas9-mediated genome editing does not necessarily affect mRNA level which was recently described (Smits et al., 2019). To examine the impact of *Myod1* editing on SCs, we noticed a robust increase of the number of FISCs (Figures 2E and S2G), in line with previous finding using *Myod1* knockout mice (Yamamoto et al., 2018). When the SCs were cultured for differentiation for 2 or 4 days, *Myogenin* or *MyHC* was found to be significantly decreased (Figures 2F and S2H), confirming a defect in myoblast differentiation caused by MYOD1 loss; but the decreases were comparable among the groups with different doses. Taken together, these results suggest the middle dose (1×10^{11} vg/mouse) of AAV9-sgRNA administered at postnatal stage elicits almost complete depletion of MYOD1 expression *in vivo*. It is worth pointing out that a much higher dose (2×10^{14} genome copies per kilogram of body weight) of AAV9 virus particles was systemically administered by intravenous injection in the study by Hinderer et al. (2018); the dosages we used were much lower and locally administered IM. Nevertheless, the possible long-term effects remain to be tested.

Use of dual sgRNAs increases the genome editing efficiency in juvenile SCs

Several studies have demonstrated that simultaneous use of dual sgRNAs can induce indels as well as large deletions at the target loci to further enhance editing efficiency (Guo et al., 2017; Johansen et al., 2017). We thus sought to develop an AAV9-dual sgRNA system expressing two sgRNAs from a single vector (Figure 2G), which was shown to display higher cleavage potential compared with sgRNAs expressed from two separate vectors (Johansen et al., 2017). Two sgRNAs (sgRNA2 and sgRNAc) were selected to remove 298 bp in the exon 1 of *Myod1* (Figures 2G and S2I). A middle dose of AAV9-dual sgMyod1 virus was injected (Figure 2H). For comparison, the same dose of single AAV9-Myod1-sgRNA2 virus was administered. Expectedly, the AAV9-dual sgMyod1 virus induced excision of the intervening sequence between the two sgRNA targeting sites (Figure S2J), which was not detected in the single sgRNA- or Ctrl virus-infected SCs. In addition, we noticed a further increase in FISC number in $Pax7^{Cas9}$ mice injected with the dual versus single sgRNA (Figure 2I). However, the expression levels of MYOD1 protein (Figures 2J and S2K), *Myod1* mRNA (Figure S2L), as well as its targets, *Myogenin* and *MyHC* (Figures 2J, 2K, and S2M), were comparable between the two groups. Subsequent deep sequencing (Figures 2L and S2N–S2P) confirmed that dual sgRNAs slightly outperformed single sgRNA in editing the *Myod1* locus (92.55% ± 0.99% versus 88.13% ± 2.23%), favoring the application of dual sgRNA strategy in subsequent investigation.

CRISPR/Cas9 fails to efficiently modify SCs at quiescent stage

We next sought to test the performance of our CRISPR/Cas9/AAV9-sgRNA system in QSCs at adult stage. To this end, we generated an inducible Cas9-expressing mouse by crossing the homozygous $Rosa26^{Cas9-EGFP}$ mouse with the $Pax7^{CreER}$ knockin mouse, which contains an insertion of the CreER coding region downstream of the *Pax7* gene; the resulting offspring were referred to as $Pax7^{ER-Cas9}$ mice (Figure 3A). Unlike the $Pax7^{Cas9}$ mice, in which Cas9 is induced in PAX7-descendant cells from the embryonic stage (Tajbakhsh, 2009), Cas9 induction in $Pax7^{ER-Cas9}$ mice can be controlled by Tmx injection, thus restricting the editing to the quiescent stage. In the first strategy, a high-dose single AAV9-sgMyod1 virus was injected IM into 4-week-old $Pax7^{ER-Cas9}$ mice followed by five consecutively intraperitoneal (IP) administrations of Tmx 2 weeks later. The mice were sacrificed for SC isolation after another 3 weeks (Figures 3B and S3A). Sufficient induction of Cas9 was confirmed (Figure 3C); successful AAV9 transduction in SCs was validated by PCR amplification of dsRed in FISC DNAs isolated from mice injected with AAV9 but not in those without AAV9 administration (Figure 3D). However, no editing event at the *Myod1* locus was detected (Figure 3E) despite *Myod1* transcript levels slightly decreased (Figure S3B); no changes in MYOD1 protein (Figure 3F), mRNA expression of *Myogenin* or *MyHC* (Figure S3B), and the SC number (Figure S3C) were observed.

Next, we performed the injection of the AAV9-sgMyod1 virus at P10 hoping the increased exposure time to sgRNA would improve AAV transduction efficiency and Cas9 editing efficiency. In this strategy, juvenile SCs were infected by the virus and a portion of them were expected to become quiescence carrying the sgRNAs (Figures 3G and S3D). Compared with the first strategy, an evident increase of dsRed signal in GFP+ SCs was observed during FACS isolation (Figures 3H and S3E), and successful AAV9 transduction was confirmed (Figure S3F). Still, no editing was evident at *Myod1* locus (Figures 3I, 3J, S3G, and S3H).

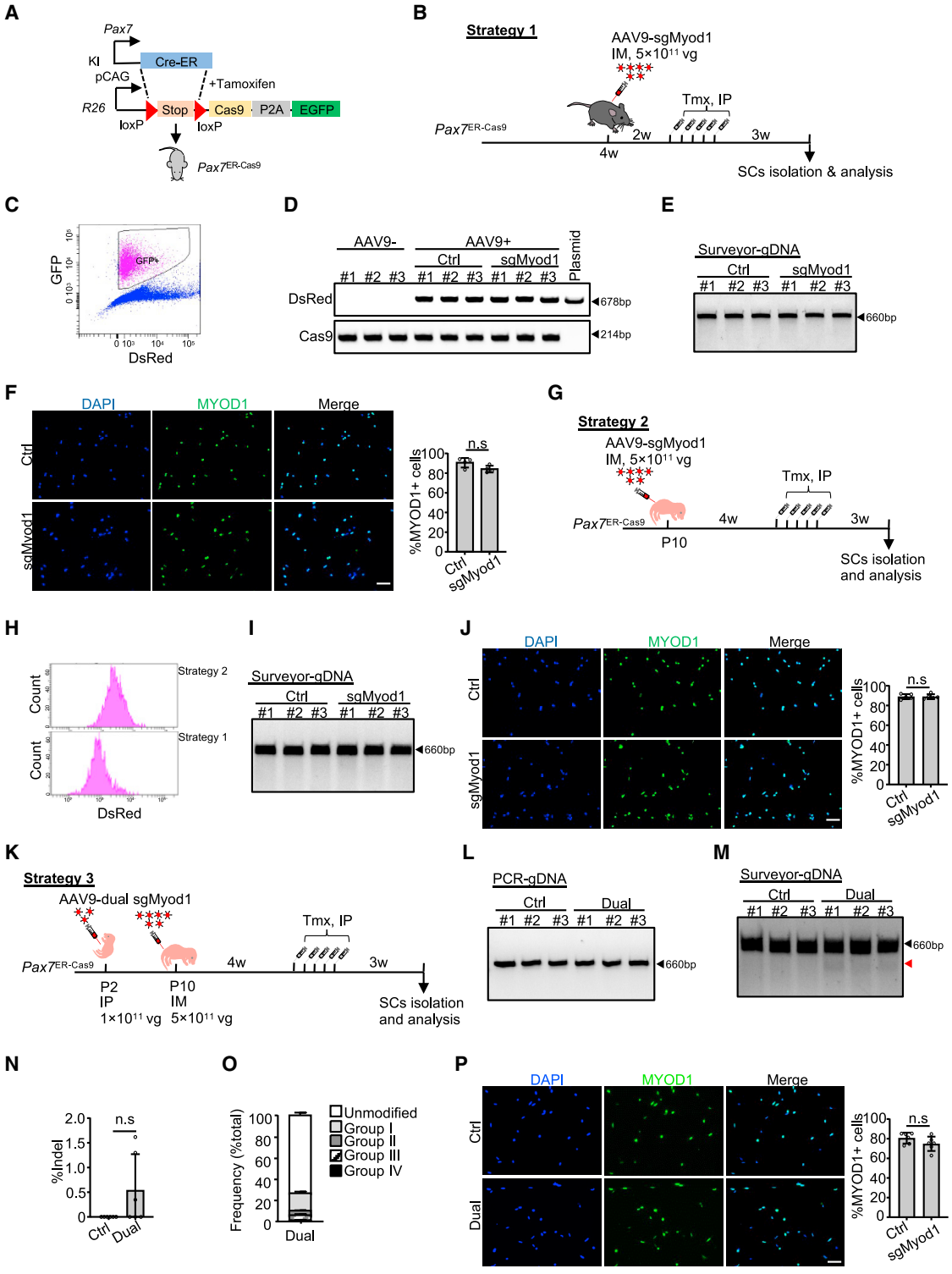

Figure 3. CRISPR/Cas9 fails to efficiently modify SCs at quiescent stage

(A) Illustration to generate the *Pax7*$^{ER-Cas9}$ mice.

(B) Illustration of the first strategy.

(C) FACS plot showing induction of Cas9-GFP expression.

(D) PCR to amplify the dsRed or Cas9 coding region. The AAV9-Myod1-sgRNA2 plasmid was used as control. n = 7 mice.

(legend continued on next page)

We next sought to determine whether the use of dual sgRNAs could possibly enhance the editing efficiency. To ensure successful AAV9 transduction into SCs, two injections were performed: a middle dose of AAV9 virus was injected via IP at P2 (Figures 3K and S3I) and reinforced by a high dose via IM at P10, which was then followed by Tmx administration 4 weeks later. The mice were sacrificed for SC isolation after another 3 weeks, and successful AAV9 transduction was confirmed (Figure S3J). Although the AAV9-dual sgMyod1 virus failed to excise the intervening sequence between the two sgRNA targeting sites (Figure 3L), Surveyor assay revealed an inconsistent editing at the *Myod1* locus (Figures 3M and 3N). Nevertheless, by deep sequencing, we determined ~27% (26.87% ± 2.15%) of the total reads were actually edited and about 1% (1.18% ± 0.37%) elicited deletions (Figures 3O, S3K, and S3L). However, we found that the above limited level of editing failed to induce obvious change of SC number (Figure S3M) or expressions of *Myod1*, *Myogenin*, or *MyHC* (Figures 3P and S3N). To speculate the possible reasons for the unsuccessful editing in QSCs, we looked into the chromatin accessibility of the *Myod1* locus as it is known that condensed heterochromatic regions are resistant to Cas9-mediated editing (Doetschman and Georgieva, 2017). However, evident H3K27ac chromatin immunoprecipitation sequencing (ChIP-seq) signals (Machado et al., 2017) were observed at the above sgRNA target sites (Figure S3O), indicating inaccessibility to Cas9 may not account for the failed editing in QSCs. Taken together, our results demonstrate that the *in vivo* CRISPR/Cas9/AAV9-sgRNA system fails to induce efficient genome editing at the *Myod1* locus in QSCs.

Key TFs regulating SC quiescence and activation are predicted through SEs

Next, we sought to extend our CRISPR/Cas9/AAV9-sgRNA system to dissect the functions of key TFs in myogenesis. Recent study has shown that key TFs bind clusters of enhancers termed super-enhancers (SEs) and that key TFs themselves are often driven by SEs, which can be used to predict key TFs (Saint-André et al., 2016). Therefore, ChIP-seq of H3K27ac was performed in FISCs from *Pax7*-nGFP mice and activated SCs (ASCs) cultured for 24 h (Figures 4A, S4A, and S4B). Enhancer constituents were then identified following the standard analysis pipeline (Peng et al., 2017) (Figure S4C; Table S1), showing dynamic remodeling of enhancer landscape during SC activation (Figure S4D; Table S1). A modified ROSE algorithm (Peng et al., 2017) was then applied to define 57 and 163 SEs in FISCs and ASCs, respectively (Figures S4E and S4F; Table S2). Based on the interconnected property between SEs and key TFs (Saint-André et al., 2016), key TFs were then predicted (Figures 4B and S4G). Ten in FISCs were defined (PAX7, RUNX1, MEF2D, CEBPB, KLF9, SOX4, ESR1, SIX1, BCL6, and RORA) and 11 in ASCs (PAX7, TGIF1, RUNX1, NFIX, MYOD1, SIX1, CEBPB, MYC, NFIA, PKNOX2, and BCL6; Figures 4B and S4E and Table S2). Of note, PAX7 was present in both FISC and ASC lists, while MYOD1 only appeared in the ASC list (Figures S4E and S4H).

Among these key TFs, BLC6 is a transcription repressor, while MYC normally functions to activate target gene expression. In muscle system, MYC is known to inhibit C2C12 differentiation through preventing myoblast fusion (Crescenzi et al., 1994), whereas BLC6 plays a pro-differentiating role by restraining apoptotic cell death (Kumagai et al., 1999). Moreover, our RNA sequencing (RNA-seq) showed these two TFs displayed distinct expression dynamics during SC lineage progression (Figure 4C): *Myc* exhibited the highest expression in FISCs and continued to decrease in ASCs and differentiated SCs (DSCs); however, *Bcl6* expression decreased slightly in ASCs versus FISCs but increased dramatically in DSCs. It is interesting that, despite the high expression of *Myc* in FISCs, no associated SE was identified (Figure S4I) thus not predicted as a key TF in FISCs. The above RNA-seq results were validated by qRT-PCR in SCs cultured for 24, 48, and 72 h, during which period SCs were activated (24 h), proliferated (48 h), and differentiated (72 h) (Figure 4D). At the protein level, the two TFs exhibited definitely

(E) Surveyor assay to detect the editing efficiency at *Myod1* locus. n = 7 mice.
(F) SCs were cultured for 2 days and IF stained for Myod1. n = 4 mice (an average of six fields/mouse). Scale bar, 50μm.
(G) Illustration of the second strategy.
(H) FACS histograms to compare the dsRed signal of the Cas9-GFP positive SCs between strategies 1 and 2.
(I) Editing efficiency was examined as in (E). n = 5 mice.
(J) SCs were cultured for 2 days and IF stained for MYOD1. n = 5 mice (an average of six fields/mouse). Scale bar, 50μm.
(K) Illustration of the third strategy.
(L) PCR analysis targeting *Myod1* locus. n = 6 mice.
(M and N) Editing efficiency was examined as in (E). The black and red arrowheads indicate wild and cleaved bands respectively (M). The frequency of indel formation was quantified (N). n = 6 mice.
(O) Distribution of the total sequencing reads in genomic DNA that showed faint editing in (N). n = 3 mice.
(P) SCs were cultured for 2 days and IF stained for MYOD1. n = 6 mice (an average of eight fields/mouse). Scale bar, 50 μm. All the bar graphs are presented as mean ± SD. ns, no significance.
See also Figure S3.

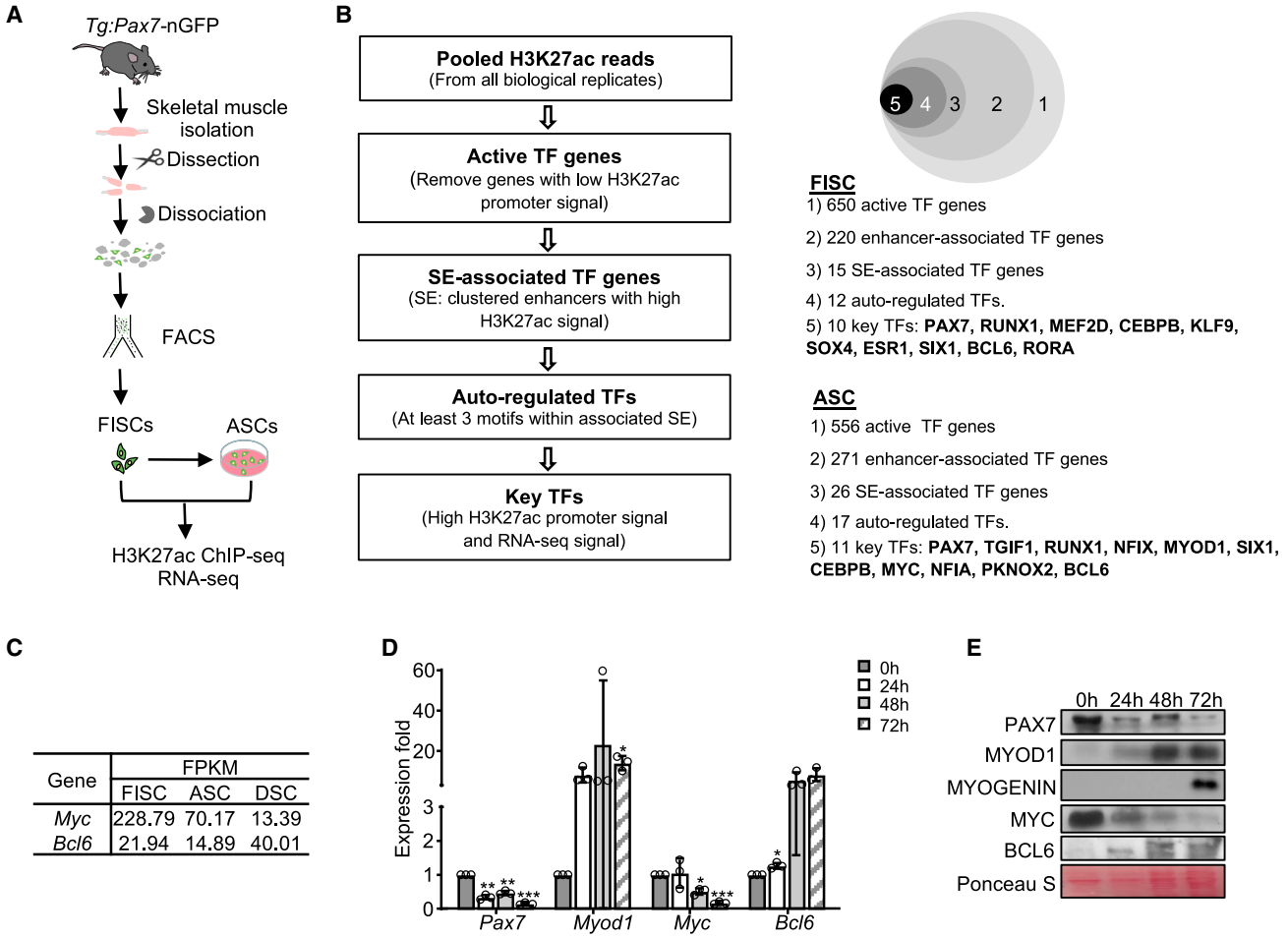

Gene	FPKM		
	FISC	ASC	DSC
Myc	228.79	70.17	13.39
Bcl6	21.94	14.89	40.01

Figure 4. Key TFs regulating SC quiescence and activation are predicted through SEs

(A) Illustration of collection of FISCs and ASCs.

(B) Left: illustration of the pipeline for predicting key TFs. Right: Venn diagram showing the identified key TFs.

(C) Expression levels of two selected key TFs examined by RNA-seq.

(D) mRNA expression of the above TFs. n = 3 independent experiments. The data were normalized to *18S* mRNA and presented as mean ± SD. *p < 0.05, **p < 0.01, ***p < 0.001.

(E) The protein levels of the above TFs.

See also Figure S4 and Tables S1 and S2.

opposite trends consistent with their mRNA changes (Figure 4E). Based on their expression dynamics and known functions, MYC and BLC6 may play different roles during SC lineage progression and were selected for further functional investigation.

CRISPR/Cas9/AAV9-sgRNA-mediated genome editing of *Myc* hinders SC activation and muscle regeneration

We next sought to validate the functionality of MYC and BLC6 in early stages of SC fate transition through leveraging our established CRISPR/Cas9/AAV9-sgRNA system. To edit *Myc*, two sgRNAs (sgRNA1 and sgRNAb) were selected (Figures 5A and S5A); the AAV9-dual sgMyc vector succeeded in excising the *Myc* locus *in vitro* (Figure S5B). Following the above established administration strategy (Figure S5C), a middle dose of the dual sgMyc virus was injected to the $Pax7^{Cas9}$ muscle at P10, which, however, led to inefficient editing (Figures S5D and S5E). Increased dose of 5×10^{11} vg/mouse (Figure 5B) yielded successful deletion of a 235 bp of the *Myc* exon (Figures 5C and S5F). Deep sequencing revealed ~83% editing at the *Myc* locus (Figures 5D and S5G) and ~18% of the total reads were detected as deletions (Figure 5D, group IV). The level of *Myc* mRNA was not significantly changed (Figure S5H), but MYC protein level was remarkably decreased (Figure 5E). We further attempted the editing in QSCs; as expected, no indel

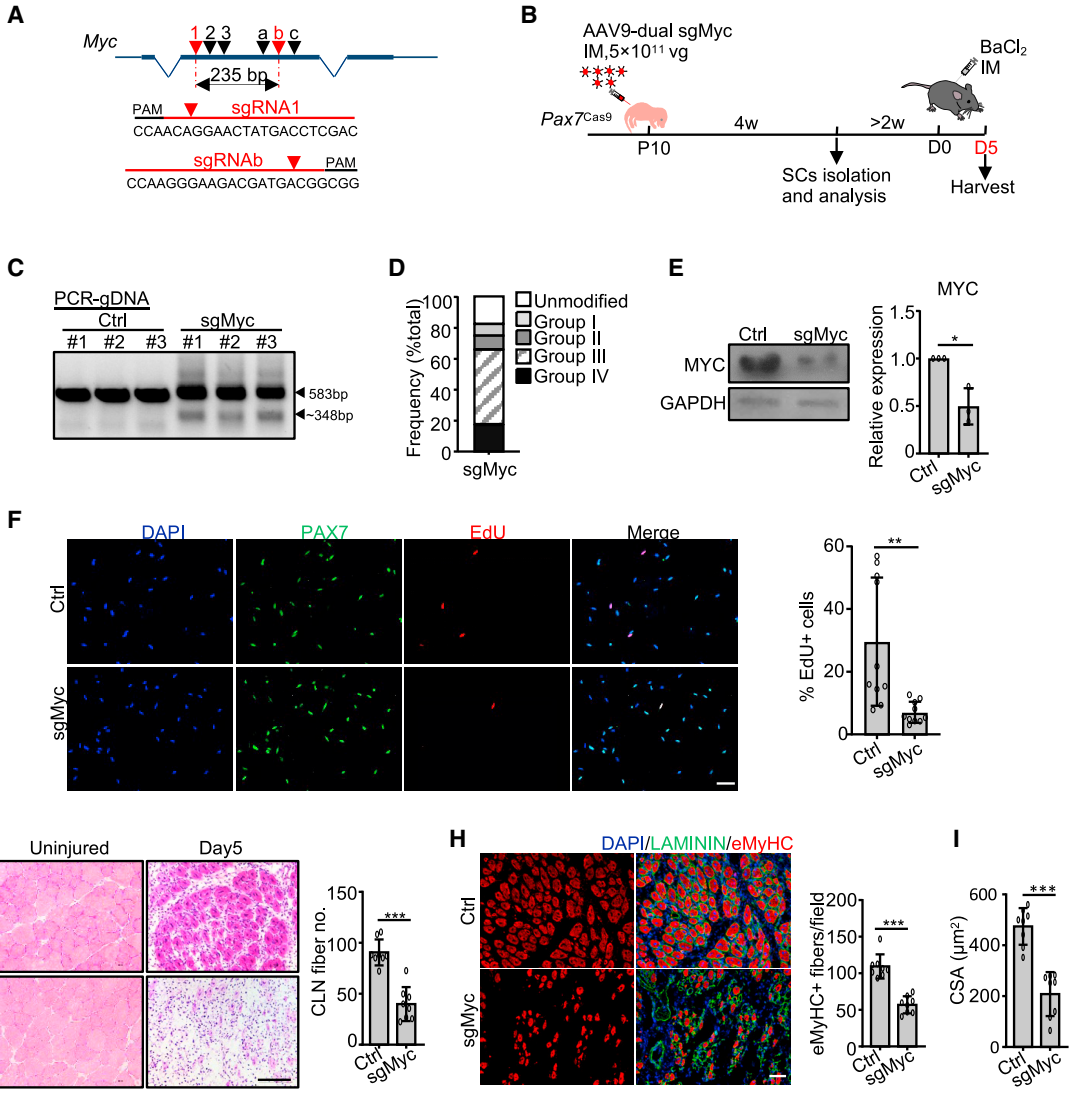

Figure 5. CRISPR/Cas9/AAV9-sgRNA-mediated genome editing of *Myc* hinders SC activation and muscle regeneration

(A) Dual sgRNAs targeting *Myc* locus.

(B) Illustration of the experimental design.

(C) PCR to test the cleavage efficiency. Wild-type (583 bp) and cleaved (~348 bp) fragments are indicated by arrowheads.

(D) Distribution of the total sequencing reads.

(E) Left: MYC protein level. Right: the band intensity. n = 3 mice.

(F) FISCs were labeled with EdU for 24 h and the percentage of EdU+ cells was quantified. n = 10 mice (an average of 25 fields/mouse). Scale bar, 50 μm.

(G) Left: H&E staining at 5 days post injury. Right: the myofibers with CLN per field. n = 8 mice (an average of six fields/mouse). Scale bar, 100 μm.

(H) Left: immunostaining of eMyHC and LAMININ. Right: the number of eMyHC+ myofibers. n = 8 mice (an average of seven fields/mouse). Scale bar, 50 μm.

(I) The CSA of the newly formed fibers with CLN. n = 8 mice. All the bar graphs are presented as mean ± SD. *p < 0.05, **p < 0.01, ***p < 0.001.

See also Figures S5 and S6.

occurrence was detected (Figures S5I and S5J) despite the sgRNA target sites appeared to be at open chromatin regions marked by H3K27ac (Figures S5K).

Next, when analyzing the impact of *Myc* editing on SCs, no obvious difference in the number of sorted SCs was detected in AAV9-dual sgMyc versus Ctrl group (Figure S5L),

suggesting the loss of MYC may not influence SC homeostasis. To characterize MYC function on SC activation, the edited SCs were cultured *in vitro* for 24 h in the presence of 5-ethynyl-2′-deoxyuridine (EdU) as it is commonly believed that it takes about 24–36 h for SCs to enter the first cell cycle and become fully activated (Rodgers et al., 2014). MYC loss led to a significant delay of SC activation (Figure 5F), suggesting that MYC protein functions to promote SC activation. The promoting effect appeared to be in discrepancy with its downregulation in ASCs versus FISCs (Figures 4C–4E); however, further examination of *Myc* expression in QSCs (obtained by prior *in situ* fixation with paraformaldehyde [PFA] before FACS, which is believed to avoid the isolation induced early activation of SCs; Machado et al., 2017) revealed it was indeed induced in FISCs versus QSCs (Figure S5M), which was also confirmed by IF staining of MYC protein (Figure S5N). To further examine whether loss of MYC impairs damage induced muscle regeneration, $Pax7^{Cas9}$ mice were administered with high doses of AAV9-dual sgMyc virus at P10 followed by $BaCl_2$ injection in the TA muscle 6 weeks later (Figure 5B). Without injury, the body weight and limb muscle weight of the mice injected with sgMyc virus did not display evident difference (Figure S5O). Moreover, the PAX7+ SC number was not affected (Figure S5P), again indicating that loss of MYC may not affect SC homeostasis in adult mice. The average fiber size in the uninjured muscles showed no difference either (Figure S5Q). However, 5 days post injury, we observed a significantly reduced number of regenerating myofibers with CLN in sgMyc versus Ctrl group (Figure 5G). Consistently, IF staining of eMyHC revealed a marked decrease in the number of newly formed fibers (Figure 5H) as well as fiber size (Figure 5I). Together, the above findings demonstrate MYC is important for SC activation and acute-injury-induced muscle regeneration.

To further demonstrate the usage of the *in vivo* genome editing system, we expanded to include BLC6. The designed dual sgRNAs yielded obvious cleavage *in vivo* (Figures S6A–S6D) but also failed to edit the *Bcl6* locus in QSCs (Figures S6E and S6F); Interestingly, different from *Myod1* and *Myc* cases, we found the sgRNA target sites were located in regions void of H3K27ac signal (Figures S6G). About 38% of indel formation was detected (Figure S6H). Similar to the *Myc* case, editing of *Bcl6* induced obvious decrease of its protein expression without altering the mRNA level (Figures S6I and S6J). Although the number of sorted FISCs was not affected (Figure S6K), editing of *Bcl6* led to accelerated SC activation (Figure S6L). However, the muscle regeneration process after acute injury appeared to be delayed (Figures S6M–S6P). We think this discrepancy may be caused by the pleiotropic roles BLC6 plays in different stages of SC lineage progression. Although it inhibits SC activation, it is known to promote myoblast differentiation (Kumagai et al., 1999); therefore, the net effect on regeneration appeared to be negative.

MYC orchestrates SC activation through impinging on 3D chromatin architecture

Next, we attempted to elucidate the mechanism underlying the above-described MYC function in SC activation. RNA-seq analysis was conducted to dissect the transcriptomic changes induced by MYC depletion in QSCs isolated from $Pax7^{Cas9}$ mice infected with sgMyc virus (Figure S7A). A total of 701 and 374 genes were up- or downregulated, respectively (Figure 6A and Table S3). The upregulated genes were highly enriched for GO terms such as "membrane" and "plasma membrane." It is known that QSCs express various glycoproteins distributed on the cell membrane as extracellular sensors to integrate signals from the niche to actively maintain SC in quiescent stage (Ancel et al., 2021). It is thus likely that loss of MYC promotes SC quiescence and delays SC early activation through increasing the expression of these glycoproteins. Additionally, among the upregulated genes, we also found *Cebpb* (Lala-Tabbert et al., 2020) and *Mexo1* (Nguyen et al., 2017) (Figure 6B), which are known to maintain SC quiescence and inhibit SC activation. The downregulated genes were not enriched for any significant GO terms (Table S3); however, some genes, for example *Dlk1*, are known to promote SC activation (Zhang et al., 2021). Moreover, the expression of some well-known MYC targets, including *Kat2a* and *Itgb4* (Kress et al., 2015) (Figure S7B), were repressed and activated respectively. Since the gene expression program is tightly orchestrated by the 3D genome conformation at multiple levels, including compartments, topologically associate domains (TADs), and chromatin loops (Ke et al., 2017), and MYC has a potential role in remodeling global genome structure (Kieffer-Kwon et al., 2017), *in situ* high-throughput chromosome conformation capture (Hi-C) was then performed in the above QSCs (Figures S7A, S7C, and S7D) to identify MYC-depletion-induced 3D genome alterations. Globally, MYC depletion resulted in a higher ratio of inter-chromosomal interactions in QSCs (Figures 6C and 6D), indicating a potential role of MYC in chromosome segregation. At the compartment level, the compartmentalization matrices displayed a similar pattern (Figure 6E), despite a mild increase being observed in long-range chromatin interactions upon MYC loss (Figures 6F and S7E), indicating MYC may promote chromatin decompaction, as suggested by a recent study (Kieffer-Kwon et al., 2017). Overall, the A and B compartments remained constant, as compartmentalization strength (Figure S7F), compartment profiles by principal component 1 (PC1) values (Figures 6G and S7G and Table S4), as well as compartment score (Figure 6H) did not

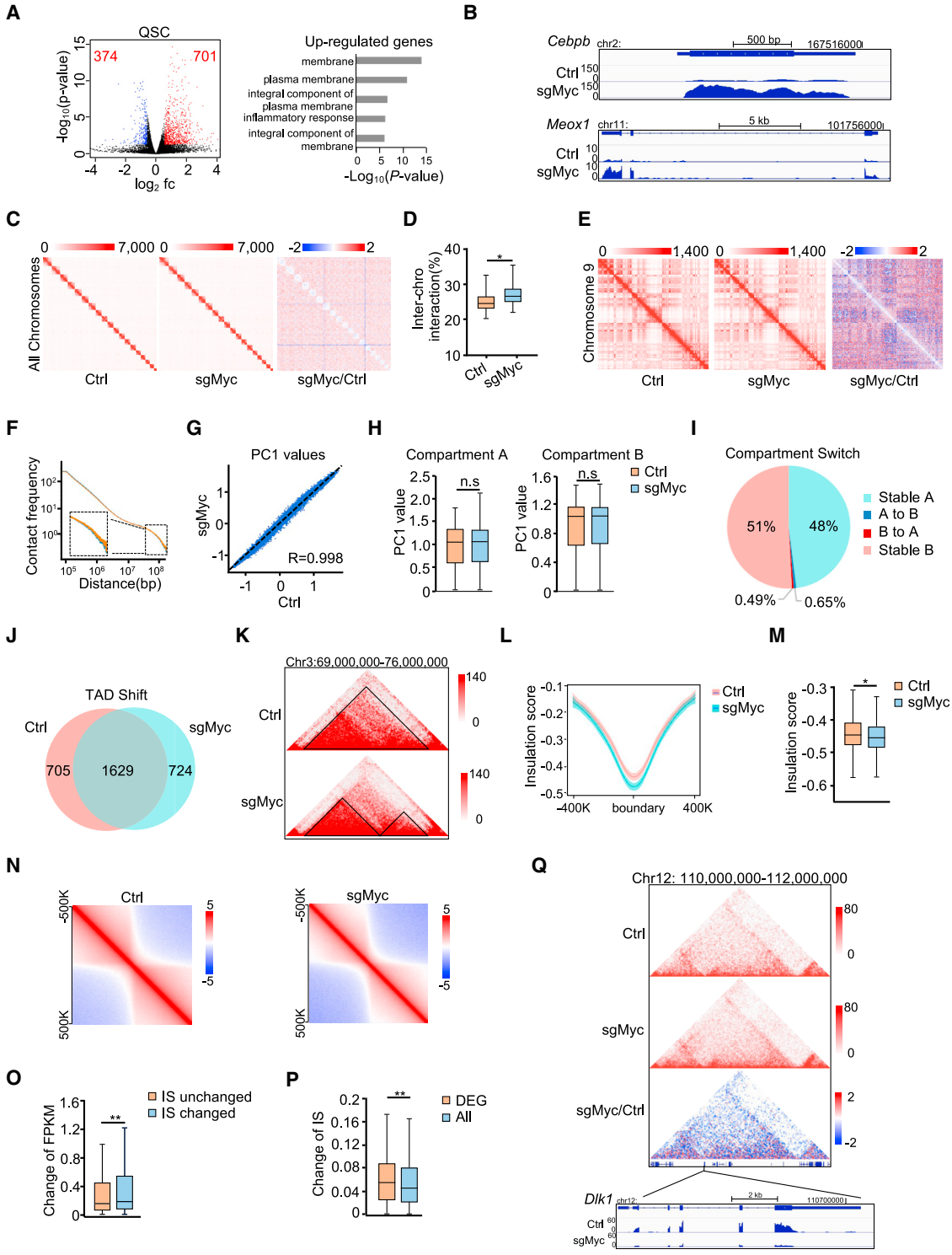

Figure 6. MYC orchestrates SC activation through impinging on 3D chromatin architecture

(A) RNA-seq for Ctrl and sgMyc QSCs. Left: DEGs were identified. Right: GO analysis of the upregulated genes. Fc, fold change.

(B) Two examples of upregulated genes.

(C) Hi-C interaction matrices in Ctrl (left) and sgMyc (middle) QSCs. Heatmap of differential inter-chromosomal interactions (right). Resolution: 5 Mb.

(legend continued on next page)

display significant alterations. Only about 0.65% of the genome switched from A compartment to B and 0.49% from B to A (Figure 6I and Table S4).

Next, a total of 2,334 and 2,353 TADs were identified in Ctrl and sgMyc groups, respectively (Figure 6J and Table S5); TAD size was largely unaltered with the median length of 720 kb (Figure S7H); and TAD numbers per chromosome were also comparable (Figure S7H). Although the majority of TADs (1,629) were stable, MYC depletion resulted in shifting of 30.2% (705) of the TADs (Figures 6J and 6K), in which cases the TADs split, merged, disappeared, built, or rearranged (Ke et al., 2017) (Figure S7I and Table S5). Interestingly, such TAD shifting was also uncovered in B cells when we examined the published Hi-C data (Kieffer-Kwon et al., 2017) (Figure S7J); a total of 2,625 TADs were identified in B cells and 38.4% (1,007) were found to be shifted upon MYC deletion. Of note, although 1,976 TAD boundaries were conservatively identified in both B cells and QSCs (Figure S7K), only 70 boundaries were changed in both cells upon MYC deletion (data not shown), indicating MYC impact on TAD boundaries may be cell type specific. Further analysis revealed that loss of MYC in QSCs caused a decrease of TAD insulation score (IS) (Figures 6L-6N), indicating strengthened boundary formation and decreased inter-TAD interactions (Figures S7L and S7M). Interestingly, intra-TAD interactions also decreased (Figure S7L). To further determine whether MYC-dependent change of TAD boundary strength correlated with disrupted expression of genes located at the boundary regions, we found that genes located within the boundaries with at least 50% IS value change (ΔIS) underwent higher expression changes upon MYC depletion compared with those residing within IS unchanged boundaries (1.44 versus 1.19) (Figure 6O); with a different cutoff of ΔIS $\geq$20%, the expression changes remained significant (1.31 versus 1.21) (Figure S7N). Furthermore, differentially expressed gene (DEG)-containing boundaries displayed higher change of IS compared with average IS change of all boundaries (Figures 6P and S7O), indicating a correlation between TAD alteration and gene expression change orchestrated by MYC in QSCs (Figure 6Q). Further GO analysis of these boundary-located DEGs revealed that they were enriched for membrane-related terms including "membrane," "potassium channel activity," and "integral component of plasma membrane" (Figure S7P and Table S6), consistent with the findings from Figure 6A and reinforcing the notion that MYC may control SC quiescence and early activation through regulating membrane-related glycoproteins. Lastly, we found 80.2% (1,005) of the H3K27ac positive peaks within the TAD boundary regions contained MYC binding motifs (Figure S7Q). Since MYC has been reported to recruit histone-modifying enzymes, including the histone acetyltransferases TIP60 and KAT2A and the serine/threonine kinase PIM1 (Kress et al., 2015), it is possible that MYC may interact with these chromatin-modifying enzymes on the open boundary regions, which subsequently affect boundary organization. In sum, our data suggest that MYC may potentially function to modulate 3D genome architecture to regulate gene expression program in SCs.

DISCUSSION

In this study, leveraging the Cas9 knockin mouse and AAV9-mediated sgRNA delivery, we documented *in vivo* genome editing by CRISPR/Cas9 in active juvenile SCs but not in quiescent SCs at adult stage. Using *Myod1* locus

(D) The ratio of inter-chromosomal in total interactions for each chromosome.
(E) Normalized interaction matrices for chromosome 9 in Ctrl (left) and sgMyc (middle) QSCs. Heatmap of differential interactions (right). Resolution: 250 kb.
(F) Overall scaling of normalized interaction frequency as a function of genomic distance in Ctrl (blue) and sgMyc (orange) QSCs.
(G) PC1 values of each compartment.
(H) Boxplots showing the compartment score of A (left) and B compartments (right).
(I) Pie chart showing compartment switching.
(J) Venn diagram showing the number of shifted TADs.
(K) Snapshot of Hi-C matrices to show TAD shift. The black triangles indicate the identified TADs.
(L) Average IS distribution around TAD boundaries (±400 kb).
(M) Boxplots showing TAD IS.
(N) Aggregate Hi-C maps of TAD borders.
(O) Boxplot showing the absolute fragments per kilobase per million (FPKM) changes for genes located within boundaries with at least 50% IS value change upon MYC depletion compared with those residing in IS unchanged boundaries.
(P) Boxplots showing the absolute IS changes for DEG-containing boundaries compared with all boundaries.
(Q) Top: snapshot of Hi-C data showing differential contact map at genomic regions encompassing *Dlk1* locus. Bottom: differential expression of *Dlk1* in QSCs determined by RNA-seq. Statistical analyses in H, M, O, and P were done by Wilcoxon rank-sum test; *$p < 0.05$, **$p < 0.01$. ns, no significance.
See also Figure S7 and Tables S3–S6.

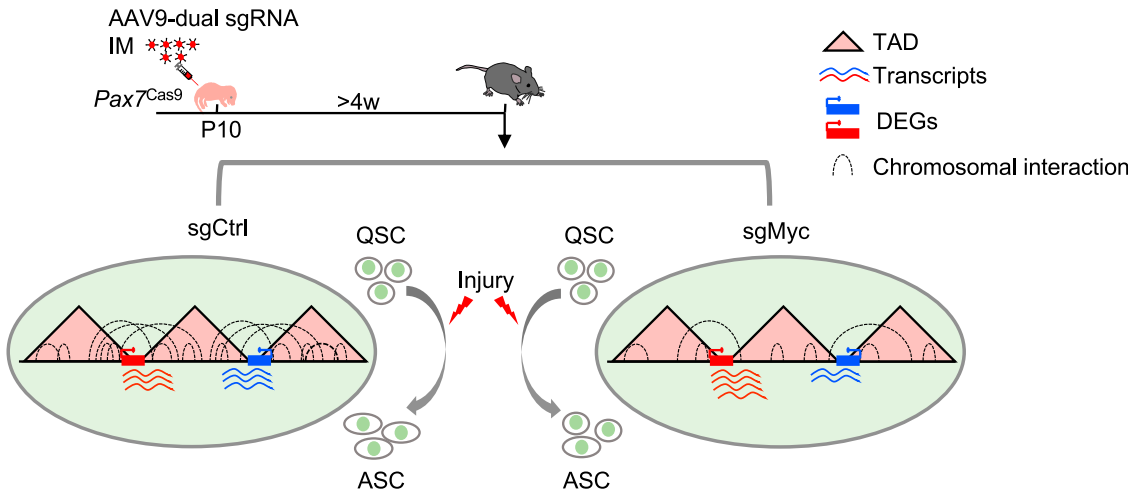

Figure 7. CRISPR/Cas9/AAV-sgRNA-mediated *in vivo* genome editing uncovers the possible role of MYC in 3D genome organization in SCs

Pax7^{Cas9} mice were administered with AAV9-dual sgRNA virus at postnatal stage to delete MYC expression in QSCs. MYC depletion results in a global strengthening of the TAD boundaries and decrease of both of the intra- and inter-TAD interactions. The change of TAD boundary strength is associated with disrupted gene expression, which may lead to delayed SC activation.

as a proof of concept, this CRISPR/Cas9/AAV9-sgRNA system efficiently introduced mutagenesis at the target locus and disrupted its expression in SCs. Application of this system on key TFs predicted by SEs, MYC, and BLC6 revealed their distinct functions in the early stage of SC activation and acute-damage-induced muscle regeneration. Further mechanistic investigation uncovered a possible role for MYC in regulating SC activation through modulating 3D genome organization (Figure 7).

One of our key findings is that the CRISPR/Cas9/AAV9-sgRNA system achieved a remarkable editing efficiency in endogenous juvenile SCs. Overall, our system manifests several advantages. The most prominent one is that it allows for manipulation of SC genomes *in situ* without requiring cell isolation or culture, thereby making it possible to study the impact on SC quiescence, homeostasis in their native niche, and early activation upon damage. On the paradigm of *Myod1* locus, it achieved up to 95% editing efficiency and nearly complete depletion of MYOD1 protein even at the low dose of AAV9-sgRNA (0.2×10^{11} vg/mouse) (Figure 2). The attempt on *Myc* locus was also successful with around 83% genome editing and a significant depletion of MYC protein. However, a high dose of AAV (5×10^{11} vg/mouse) was necessitated for *Myc* locus. The editing efficiency on *Bcl6* (38%) was not high even with the use of the high dose of virus and dual sgRNAs, suggesting that the editing efficiency is locus dependent, which may be due to the inherent quality of different protospacer sequences or the chromatin state of each locus (Doetschman and Georgieva, 2017).

It is foreseeable that our system will accelerate the pace at which gene function and interaction can be interrogated in endogenous SCs compared with commonly employed transgenic and gene knockout-based models. Traditionally, it is time consuming and expensive to generate knockout mice, and this shortcoming would be exacerbated when multiple genes need to be disrupted simultaneously. However, in our system, the entire procedure from sgRNA selection to phenotypic dissection only takes several weeks. In addition, our system can be adapted to enable rapid and direct *in vivo* screening of candidate and novel targets suspected to influence SC phenotypes. The ability to achieve multiplex genetic perturbations using the Cas9 mouse also enables the possibility of interrogating multigenic effects. In addition to coding genes, this system can also be used to interrogate non-coding genome such as enhancers and long non-coding RNAs (lncRNAs). For example, in a recent study (Zhao et al., 2019), we applied it to edit an enhancer RNA (eRNA) in skeletal muscle, which facilitated the investigation of the eRNA function in regulating myoblast differentiation.

Of note, this system has several limitations. One caveat is that the AAV9 administration can also edit muscle fibers. Since PAX7 expression emerges as early as embryonic day 10.5 (E10.5) in muscle progenitor cells to drive the formation of muscle compartments (Tajbakhsh, 2009), Cas9 is expressed not only in SCs but also in the fibers of *Pax7*^{Cas9} mice. We attempted to solve this problem by using inducible *Pax7*$^{ER-Cas9}$ mice that will allow SC restricted expression of Cas9, but the results are not compelling at the current stage. Second, this system does not generate a uniform

knockout mouse. Although the transduction efficiency appeared to be close to 100% (Figure S1H), the editing efficiency per SC and the editing events largely varied (Figures S2D and S5G), leading to mosaic mutagenesis. Mosaic editing for some genes may not be sufficient to elicit any phenotypical alterations, in which case the traditional knockout models are needed to confirm the findings.

Another unexpected observation in our study is the incompetence of CRISPR/Cas9 to edit QSCs. The inefficient transduction of AAV virus into the adult SCs was thought to be the reason (Arnett et al., 2014). However, findings from detecting an AAV9-specific element using a sensitive PCR-based method (Figure 3D) demonstrated successful transduction of AAV9 into QSCs, which was substantiated by two recent studies showing high transduction efficiency of multiple AAV serotypes to adult SCs by a Cre/lox fluorescent reporter tracking system (Goldstein et al., 2019; Nance et al., 2019). Still, no obvious editing was achieved after Tmx induction of Cas9 expression (Figure 3E). In a second strategy, we also attempted to inject the AAV9 virus at juvenile stage followed by Cas9 induction after the infected SCs became quiescence (Figure 3G). Augmented transduction efficiency was achieved (Figures 3H and S3E), but the editing remained unsuccessful at all three loci, *Myod1* (Figure 3I), *Myc* (Figures S5I and S5J), and *Bcl6* (Figures S6E and S6F). On the *Myod1* locus, however, we noticed a weak editing identified by in-depth sequencing when dual sgRNAs were applied (Figure 3O). Since active myogenesis may occur in adult mice to repair subtle injuries routinely happening during normal muscle activity (Ancel et al., 2021), we cannot rule out the possibility that the observed weak editing at the *Myod1* locus may happen in activated SCs but not in QSCs. Altogether, our findings suggest insufficient copy of sgRNAs was not the reason for the failed editing. Cas9 inaccessibility to condensed heterochromatin regions may cause failed editing (Doetschman and Georgieva, 2017); however, the sgRNA target sites for both *Myod1* (Figure S3O) and *Myc* (Figure S5K) are located at accessible DNA regions. Another possibility is that the amount of Cas9 in the heterogeneous *Pax7*$^{ER-Cas9}$ mice used in our study may not be sufficient to induce the editing, as it has been shown that the concentration of Cas9 is critical for efficient editing (Doetschman and Georgieva, 2017). This puzzle thus remains to be answered in the future.

Lastly, leveraging the system, our study unraveled previously uncharacterized functions of two key TFs, MYC and BLC6, in early stages of SC activation. Loss of MYC led to evident impairment of SC activation, thus delaying acute-injury-induced regenerating process. Taking advantage of the recent developed *in situ* fixation method (Machado et al., 2017), we conducted RNA-seq and Hi-C analyses in QSCs. Our data for the first time presented a global change of 3D chromatin structure induced by MYC depletion in QSCs. Specifically, at the TAD level, we found the insulation strength of TADs, especially those containing DEGs, was dramatically altered upon MYC depletion. Our findings thus provide new insights into MYC regulation of the 3D genome, which may render its ability to modulate transcriptional program during SC activation (Figure 7). Future efforts will be needed to tease out how MYC orchestrates TAD organization through direct binding to TAD boundaries. Compared with MYC, loss of BLC6, on the other hand, slightly promoted SC activation.

In summary, our study revealed robust genome editing in active juvenile SCs but not QSCs using the Cas9 knockin mouse line in conjunction with AAV9-mediated sgRNA delivery. Importantly, we generated a versatile platform that allows efficient genome modification in endogenous SCs. Further application of this system enabled dissecting the functionality of key TFs in SC activation and muscle regeneration.

EXPERIMENTAL PROCEDURES

For further details, see supplemental experimental procedures.

Mice

All animal experiments were performed according to guidelines for experimentation with laboratory animals set in institutions and approved by the Chinese University of Hong Kong (CUHK) Animal Ethics Committee.

SC isolation, culture, and EdU incorporation assay

SCs were isolated from *Pax7*-nGFP, *Pax7*^{Cas9}, or *Pax7*$^{ER-Cas9}$ mice by the FACS method based on GFP signal as reported previously (Machado et al., 2017).

sgRNA design, selection, and Surveyor nuclease assay

Site-specific sgRNAs were predicted using the Web tool Crispor (http://crispor.tefor.net/). Surveyor nuclease assay was conducted according to the manufacturer's protocol.

AAV9 virus production, purification, and injection

AAV9 virus particles were produced in HEK293FT cells by the triple transfection method.

qRT-PCR

Total RNAs from cells were extracted using TRIzol reagent (Life Technologies) according to the manufacturer's instructions.

RNA-seq and data analysis

RNA-seq was performed as described previously (Zhao et al., 2019).

ChIP-seq and data analysis

ChIP-seq and the data analysis were performed following the procedures described previously (Peng et al., 2017).

Hi-C and data analysis

The *in situ* Hi-C libraries were prepared as previously reported (Ke et al., 2017).

Deep sequencing

Deep sequencing was performed as previously described (Johansen et al., 2017).

Statistical analysis

All the data are presented as the mean ± standard error of the mean (SD). All tests were two sided, and $p < 0.05$ was considered statistically significant.

Data and code availability

The accession code of the sequencing data used in this study is Gene Expression Omnibus (GEO): GSE134529.

SUPPLEMENTAL INFORMATION

Supplemental information can be found online at https://doi.org/10.1016/j.stemcr.2021.08.011.

AUTHOR CONTRIBUTIONS

H.W., H.S., L.H., Y.D., and Y.Z. conceived and designed the experiments. L.H., Y.Z., K.K.S., Y.L., Z.H., and X.C. performed the experiments. Y.D., X.L.P., and J.Y. analyzed the data. H.W. and L.H. wrote the paper. H.W., H.S., L.H., Y.D., and Y.Z. reviewed and edited the manuscript.

CONFLICT OF INTERESTS

The authors declare no competing interests.

ACKNOWLEDGMENTS

This work was supported by General Research Funds (GRF) from the Research Grants Council (RGC) of the Hong Kong Special Administrative Region (14116918, 14120420, and 14120619 to H.S.; 14115319, 14100018, 14100620, 14106117 and 14106521 to H.W.); the National Natural Science Foundation of China (NSFC) to H.W. (Project code: 31871304); Collaborative Research Fund (CRF) from RGC to H.W. (C6018-19GF); NSFC/RGC Joint Research Scheme to H.S. (Project code: N_CUHK 413/18); Hong Kong Epigenomics Project (EpiHK) Fund to H.W. and H.S.; Area of Excellence Scheme (AoE) from RGC (Project number: AoE/M-402/20).

Received: December 30, 2020
Revised: August 18, 2021
Accepted: August 18, 2021
Published: September 16, 2021

REFERENCES

Aloisio, G.M., Nakada, Y., Saatcioglu, H.D., Peña, C.G., Baker, M.D., Tarnawa, E.D., Mukherjee, J., Manjunath, H., Bugde, A., and Sengupta, A.L. (2014). PAX7 expression defines germline stem cells in the adult testis. J. Clin. Invest. *124*, 3929–3944.

Ancel, S., Stuelsatz, P., and Feige, J.N. (2021). Muscle stem cell quiescence: controlling stemness by staying asleep. Trends Cell Biol. *31*, 556–568.

Arnett, A.L., Konieczny, P., Ramos, J.N., Hall, J., Odom, G., Yablonka-Reuveni, Z., Chamberlain, J.R., and Chamberlain, J.S. (2014). Adeno-associated viral vectors do not efficiently target muscle satellite cells. Mol. Ther. Methods Clin. Dev. *1*, 14038.

Crescenzi, M., Crouch, D.H., and Tatò, F. (1994). Transformation by myc prevents fusion but not biochemical differentiation of C2C12 myoblasts: mechanisms of phenotypic correction in mixed culture with normal cells. J. Cell Biol. *125*, 1137–1145.

Doetschman, T., and Georgieva, T. (2017). Gene editing with CRISPR/Cas9 RNA-directed nuclease. Circ. Res. *120*, 876–894.

Goldstein, J.M., Tabebordbar, M., Zhu, K., Wang, L.D., Messemer, K.A., Peacker, B., Kakhki, S.A., Gonzalez-Celeiro, M., Shwartz, Y., and Cheng, J.K. (2019). In situ modification of tissue stem and progenitor cell genomes. Cell Rep. *27*, 1254–1264.e7.

Guo, Y., VanDusen, N.J., Zhang, L., Gu, W., Sethi, I., Guatimosim, S., Ma, Q., Jardin, B.D., Ai, Y., and Zhang, D. (2017). Analysis of cardiac myocyte maturation using CASAAV, a platform for rapid dissection of cardiac myocyte gene function in vivo. Circ. Res. *120*, 1874–1888.

Hinderer, C., Katz, N., Buza, E.L., Dyer, C., Goode, T., Bell, P., Richman, L.K., and Wilson, J.M. (2018). Severe toxicity in nonhuman primates and piglets following high-dose intravenous administration of an adeno-associated virus vector expressing human SMN. Hum. Gene Ther. *29*, 285–298.

Hosoyama, T., Nishijo, K., Garcia, M.M., Schaffer, B.S., Ohshima-Hosoyama, S., Prajapati, S.I., Davis, M.D., Grant, W.F., Scheithauer, B.W., and Marks, D.L. (2010). A postnatal Pax7+ progenitor gives rise to pituitary adenomas. Genes Cancer *1*, 388–402.

Johansen, A.K., Molenaar, B., Versteeg, D., Leitoguinho, A.R., Demkes, C., Spanjaard, B., de Ruiter, H., Akbari Moqadam, F., Kooijman, L., and Zentilin, L. (2017). Postnatal cardiac gene editing using CRISPR/Cas9 with AAV9-mediated delivery of short guide RNAs results in mosaic gene disruption. Circ. Res. *121*, 1168–1181.

Ke, Y., Xu, Y., Chen, X., Feng, S., Liu, Z., Sun, Y., Yao, X., Li, F., Zhu, W., and Gao, L. (2017). 3D chromatin structures of mature gametes and structural reprogramming during mammalian embryogenesis. Cell *170*, 367–381.e20.

Kieffer-Kwon, K.-R., Nimura, K., Rao, S.S.P., Xu, J., Jung, S., Pekowska, A., Dose, M., Stevens, E., Mathe, E., Dong, P., et al. (2017). Myc regulates chromatin decompaction and nuclear architecture during B cell activation. Mol. Cell *67*, 566–578.e10.

Kress, T.R., Sabò, A., and Amati, B. (2015). MYC: connecting selective transcriptional control to global RNA production. Nat. Rev. Cancer *15*, 593–607.

Kumagai, T., Miki, T., Kikuchi, M., Fukuda, T., Miyasaka, N., Kamiyama, R., and Hirosawa, S. (1999). The proto-oncogene Bcl6 inhibits apoptotic cell death in differentiation-induced mouse myogenic cells. Oncogene *18*, 467–475.

Lala-Tabbert, N., AlSudais, H., Marchildon, F., Fu, D., and Wiper-Bergeron, N. (2020). CCAAT/enhancer binding protein β

promotes muscle stem cell quiescence through regulation of quiescence-associated genes. Stem Cells *39*, 345–357.

Machado, L., de Lima, J.E., Fabre, O., Proux, C., Legendre, R., Szegedi, A., Varet, H., Ingerslev, L.R., Barrès, R., and Relaix, F. (2017). In situ fixation redefines quiescence and early activation of skeletal muscle stem cells. Cell Rep. *21*, 1982–1993.

Nance, M.E., Shi, R., Hakim, C.H., Wasala, N.B., Yue, Y., Pan, X., Zhang, T., Robinson, C.A., Duan, S.X., and Yao, G. (2019). AAV9 edits muscle stem cells in normal and dystrophic adult mice. Mol. Ther. *27*, 1568–1585.

Nguyen, P.D., Gurevich, D.B., Sonntag, C., Hersey, L., Alaei, S., Nim, H.T., Siegel, A., Hall, T.E., Rossello, F.J., and Boyd, S.E. (2017). Muscle stem cells undergo extensive clonal drift during tissue growth via Meox1-mediated induction of G2 cell-cycle arrest. Cell Stem Cell *21*, 107–119.e6.

Peng, X.L., So, K.K., He, L., Zhao, Y., Zhou, J., Li, Y., Yao, M., Xu, B., Zhang, S., and Yao, H. (2017). MyoD-and FoxO3-mediated hotspot interaction orchestrates super-enhancer activity during myogenic differentiation. Nucleic Acids Res. *45*, 8785–8805.

Platt, R.J., Chen, S., Zhou, Y., Yim, M.J., Swiech, L., Kempton, H.R., Dahlman, J.E., Parnas, O., Eisenhaure, T.M., and Jovanovic, M. (2014). CRISPR-Cas9 knockin mice for genome editing and cancer modeling. Cell *159*, 440–455.

Rodgers, J.T., King, K.Y., Brett, J.O., Cromie, M.J., Charville, G.W., Maguire, K.K., Brunson, C., Mastey, N., Liu, L., and Tsai, C.-R. (2014). mTORC1 controls the adaptive transition of quiescent stem cells from G 0 to G Alert. Nature *510*, 393–396.

Saint-André, V., Federation, A.J., Lin, C.Y., Abraham, B.J., Reddy, J., Lee, T.I., Bradner, J.E., and Young, R.A. (2016). Models of human core transcriptional regulatory circuitries. Genome Res. *26*, 385–396.

Smits, A.H., Ziebell, F., Joberty, G., Zinn, N., Mueller, W.F., Clauder-Münster, S., Eberhard, D., Savitski, M.F., Grandi, P., and Jakob, P. (2019). Biological plasticity rescues target activity in CRISPR knock outs. Nat. Methods *16*, 1087–1093.

Tabebordbar, M., Zhu, K., Cheng, J.K., Chew, W.L., Widrick, J.J., Yan, W.X., Maesner, C., Wu, E.Y., Xiao, R., and Ran, F.A. (2016). In vivo gene editing in dystrophic mouse muscle and muscle stem cells. Science *351*, 407–411.

Tajbakhsh, S. (2009). Skeletal muscle stem cells in developmental versus regenerative myogenesis. J. Intern. Med. *266*, 372–389.

Yamamoto, M., Legendre, N.P., Biswas, A.A., Lawton, A., Yamamoto, S., Tajbakhsh, S., Kardon, G., and Goldhamer, D.J. (2018). Loss of MyoD and Myf5 in skeletal muscle stem cells results in altered myogenic programming and failed regeneration. Stem Cell Reports *10*, 956–969.

Zhang, L., Kubota, M., Nakamura, A., Kaji, T., Seno, S., Uezumi, A., Andersen, D.C., Jensen, C.H., and Fukada, S. (2021). Dlk1 regulates quiescence in calcitonin receptor-mutant muscle stem cells. Stem Cells *39*, 306–317.

Zhao, Y., Zhou, J., He, L., Li, Y., Yuan, J., Sun, K., Chen, X., Bao, X., Esteban, M.A., Sun, H., et al. (2019). MyoD induced enhancer RNA interacts with hnRNPL to activate target gene transcription during myogenic differentiation. Nat. Commun. *10*, 5787.

Stem Cell Reports, Volume *16*

Supplemental Information

CRISPR/Cas9/AAV9-mediated *in vivo* editing identifies MYC regulation of 3D genome in skeletal muscle stem cell

Liangqiang He, Yingzhe Ding, Yu Zhao, Karl K. So, Xianlu L. Peng, Yuying Li, Jie Yuan, Zhiming He, Xiaona Chen, Hao Sun, and Huating Wang

Supplemental Information

List of Supplemental Figures

List of Supplemental Tables

Supplemental Experimental Procedures

Supplemental References

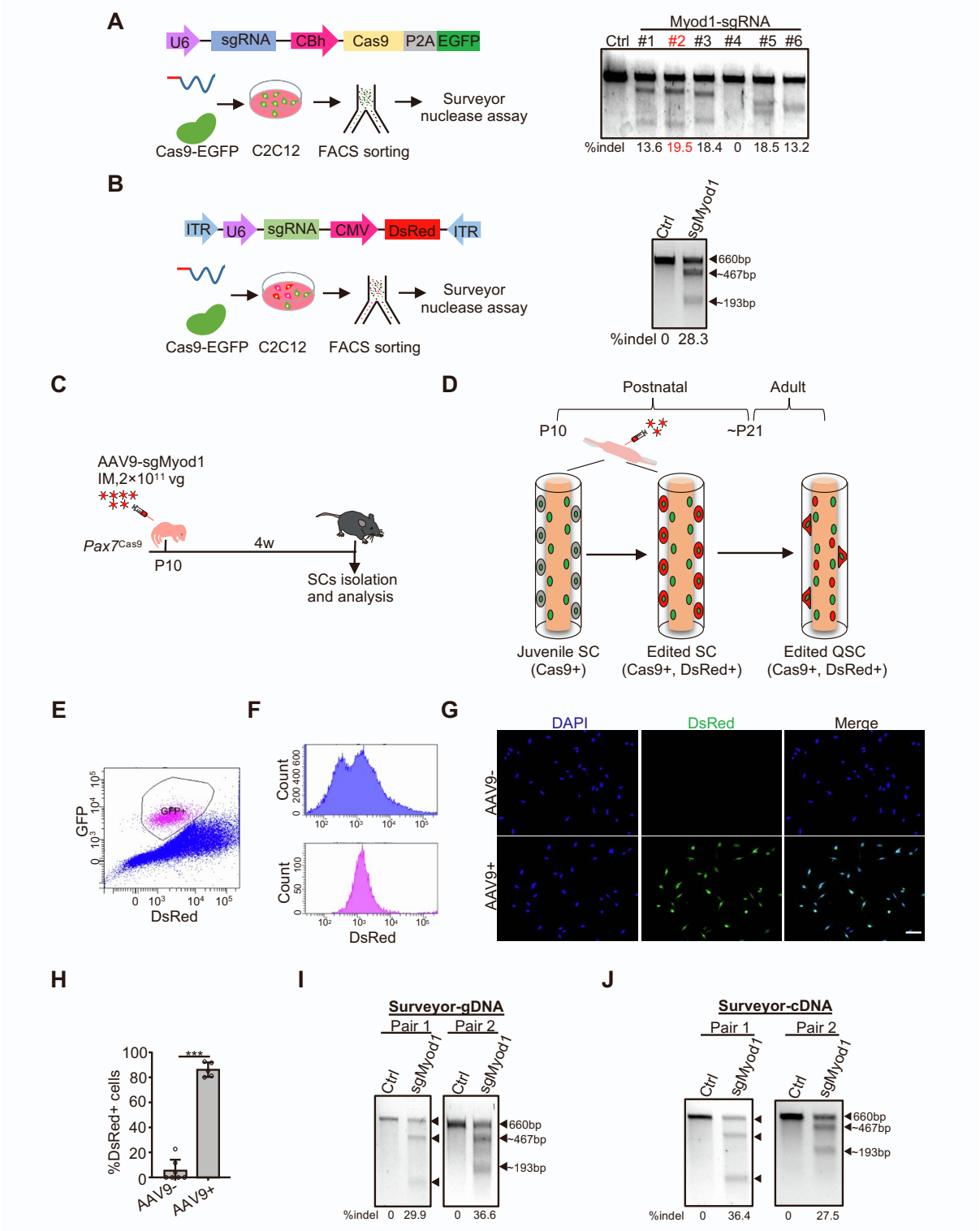

Figure S1. CRISPR/Cas9 in conjunction with AAV9 mediated sgRNAs delivery yields robust editing in juvenile SCs. Related to Figure 2. (**A**) Left: schematic illustration of the sgRNA-Cas9 expressing vector (Upper panel) and the *in vitro* sgRNA selection assay (Lower panel). SgRNA-Cas9 expressing plasmid was transfected into C2C12 myoblasts; positively transfected cells were sorted out by GFP expression one day after transfection and cultured for another two days before Surveyor nuclease assay. Right: agarose gel image showing the result of Surveyor nuclease assay on *Myod1* locus. The percentage of indel formation is shown. SgRNA2 with the highest frequency of indel

formation is indicated in red. (**B**) Testing of AAV9-Myod1-sgRNA2 vector in C2C12 myoblasts. SgRNA2 was cloned in the AAV9-sgRNA vector and transfected into C2C12 cells together with a Cas9-EGFP expressing plasmid (pX458). Positively transfected cells were FACS isolated based on GFP and DsRed expression and cultured for another two days before Surveyor nuclease assay. AAV9-sgRNA backbone without sgRNA insertion was used as a control. Wild type (660 bp) and cleaved bands (~467 bp/193 bp) by Surveyor are indicated by arrowheads. The percentage of indel formation is shown. (**C**) Schematic illustration of the experimental design for AAV administration and SC isolation & analysis. (**D**) Diagram to show the strategy of CRISPR/Cas9/AAV9 mediated *in vivo* editing of *Myod1* in juvenile SCs. AAV9-sgMyod1 virus was intramuscularly (IM) injected into the *Pax7*^{Cas9} mice at P10 to edit the juvenile SCs actively proliferating during the postnatal myogenesis. Upon the termination of the postnatal myogenesis around P21, a portion of the edited cells was expected to return quiescence carrying the editing. (**E**) FACS plot showing the gating strategy to sort out SCs from *Pax7*^{Cas9} mice based on GFP signal four weeks after AAV9-sgMyod1 virus injection. (**F**) Histogram to show the DsRed signal (Upper panel) for all the input cells in Figure S1E. The isolated Cas9-GFP+ SCs were located in the DsRed high population (Lower panel). (**G-H**) FISCs from the AAV9 injected mice were seeded for 24 hrs and IF stained for DsRed (G). SCs from *Pax7*^{Cas9} mice without AAV9 virus infection (AAV9-) were used as a control. The percentage of DsRed positive cells was quantified from at least five randomly selected fields (H). Scale bar, 50 μm. The bar graph presents mean ± s.d. ***P<0.001. (**I**) Genomic DNAs (gDNA) from FISCs of the *Pax7*^{Cas9} mice administrated with AAV9-sgMyod1 viruses were subject to Surveyor assay to test the frequency of indel formation at *Myod1* locus. Wild type (660 bp) and cleaved bands (~467 bp/193 bp) by Surveyor are shown by arrowheads. The percentage of indel formation is shown. n = 2 mice per group. (**J**) SCs isolated from the above mice were cultured for four days and *Myod1* transcripts were subject to Surveyor assay to test the frequency of indel formation at *Myod1* locus. Wild type (660 bp) and cleaved bands (~467 bp/193 bp) by Surveyor are shown by arrowheads. The percentage of indel formation is shown. n = 2 mice per group.

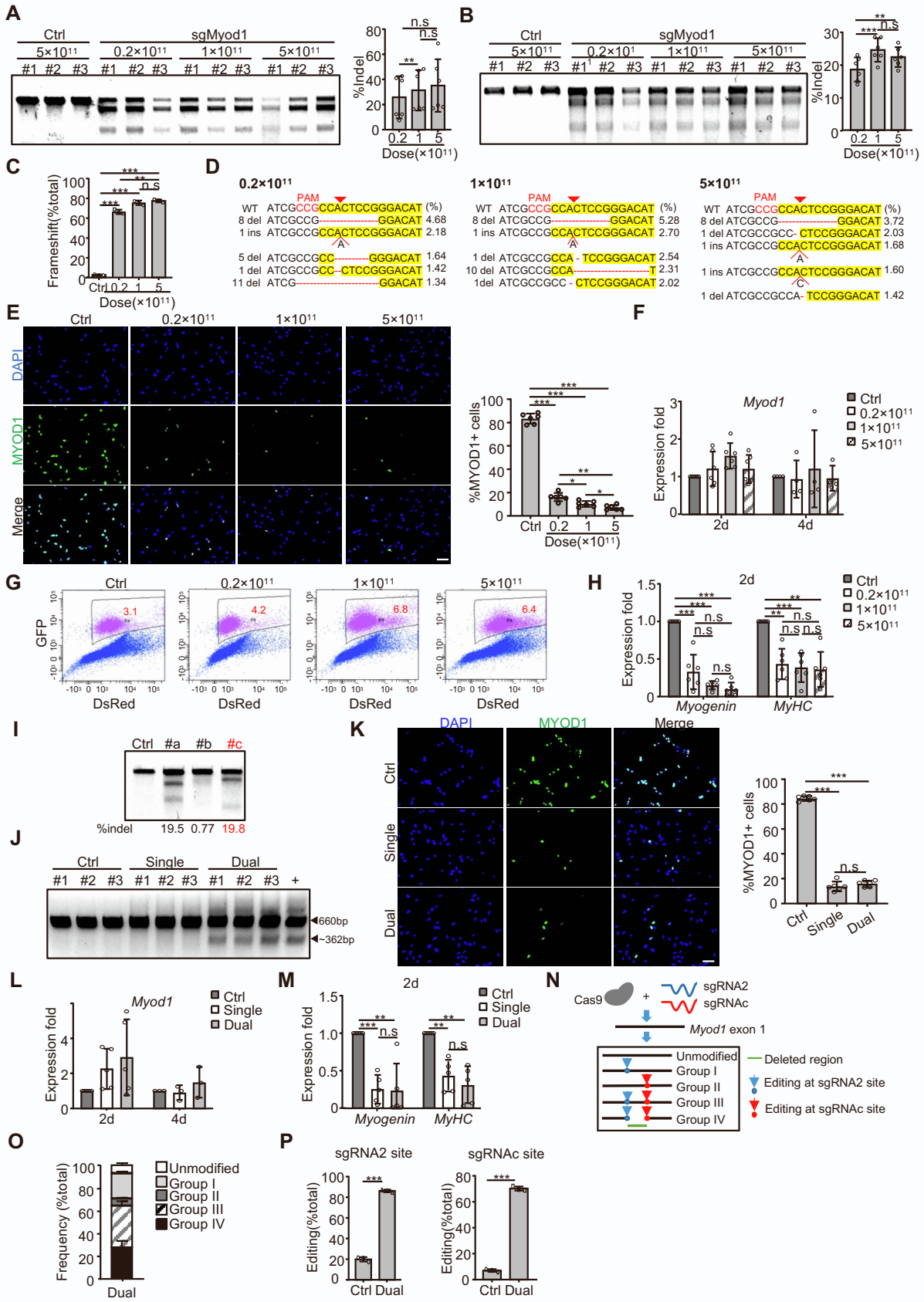

Figure S2. Effect of AAV9 dosage and dual sgRNAs on the CRISPR/Cas9 mediated genome editing in juvenile SCs. Related to Figure 2. (**A**) Left: Genomic DNAs from SCs of *Pax7*^{Cas9} mice administrated with different doses of AAV9-sgMyod1 virus were subject to Surveyor assay to test the

frequency of indel formation at *Myod1* locus. Right: The percentage of indel formation was quantified. n = 6 mice per group. (**B**) Left: SCs isolated from *Pax7*^{Cas9} mice administrated with different doses of the AAV9-sgMyod1 viruses were cultured for two days and Surveyor assay was performed to examine the editing efficiency in *Myod1* transcripts. Right: the indel occurrence was estimated. n = 6 mice per group. (**C**) Quantification of the frameshift mutations determined by deep sequencing of the genomic DNAs from SCs of the *Pax7*^{Cas9} mice administrated with different doses of AAV9-sgMyod1 viruses. The percentage was calculated as the ratio of frameshift mutations to the total reads and presented as mean ± s.d. n = 3 mice per group. (**D**) The five most frequently detected indel classes under each dose of AAV9-sgMyod1 virus are shown. The percentage is calculated as the ratio of reads for each indel class to the total edited reads. The indels included small deletions and +1 bp insertion at target site and the patterns were similar among different doses, which is in agreement with a prior report showing that the repair outcomes of CRIPSR/Cas9 mediated genome editing are not random (van Overbeek et al., 2016). (**E**) Left: the above SCs were cultured for two days and IF stained for MYOD1 protein. Right: the number of positively stained cells was counted. n = 6 mice per group. For each mouse, an average of 9 randomly selected fields were quantified. Scale bar, 50 μm. (**F**) The above SCs were cultured for two or four days and *Myod1* mRNA expression was detected by qRT-PCR (n = 4 to 6 mice per group). (**G**) Representative FACS plots showing the percentage of GFP+ SCs (indicated as red) isolated from *Pax7*^{Cas9} mice administrated with different doses of AAV9-sgMyod1 viruses. (**H**) The above isolated SCs were cultured for two days and the relative expression of *Myogenin* or *MyHC* was detected by qRT-PCR. n = 6 mice per group. (**I**) *In vitro* screening of sgRNAs targeting downstream of *Myod1* exon 1 by Surveyor nuclease assay in C2C12 myoblasts. The percentage of indel formation is presented. SgRNAc selected for *in vivo* study is marked in red. (**J**) PCR analysis to test the cleavage efficiency at *Myod1* locus in FISCs from mice injected with Ctrl/Single/Dual-sgRNA viruses. DNAs from C2C12 cells co-transfected with Cas9-expressing plasmid (pX458) and AAV9-dual sgMyod1 vector were used as positive control. Wild type (660 bp) and cleaved bands (~362 bp) are shown by arrowheads. (**K**) Left: SCs isolated from *Pax7*^{Cas9} mice administrated with middle dose of single/dual AAV9-sgMyod1 viruses were cultured for two days and IF stained for MYOD1. Right: the number of positively stained cells was counted. n = 6 mice per group. For each mouse, an average of 8 randomly selected fields were quantified. Scale bar, 50 μm. (**L**) Relative expressions of *Myod1* in the above SCs cultured for two or four days were determined by qRT-PCR (n = 3 to 5 mice per group). (**M**) Relative expression of *Myogenin* and *MyHC* in the above SCs cultured for two days were determined by qRT-PCR. n = 5 mice per group. (**N**) Schematic illustration to show non-homologous end joining (NHEJ) repair of double-strand breaks (DSBs) induced by AAV9-dual sgMyod1 (Guo et al., 2018). The edited products were divided into four groups based on whether the indels formed at either sgRNA or both target sites. Group I: editing at sgRNA2 site only; II: sgRNAc site only; III: individually at sgRNA2 and sgRNAc site; IV: simultaneously at both sites to cause deletion. (**O**) Distribution of the total sequencing reads in the dual sgRNAs group. About 27% of the total reads were detected as deletion. (**P**) The editing efficiency at sgRNA2 and sgRNAc sites in dual sgRNAs infected FISCs was determined by deep sequencing. SgRNA2 and sgRNAc yielded 86.2% and 70.21% indel formation respectively. The percentage was calculated as the ratio of the edited reads to the total reads. n=3 per group. All qRT-PCR data were normalized to *18S* or *Gapdh* mRNA. All the bar graphs are presented as mean ± s.d. *P<0.05, **P<0.01, ***P<0.001. ns, no significance.

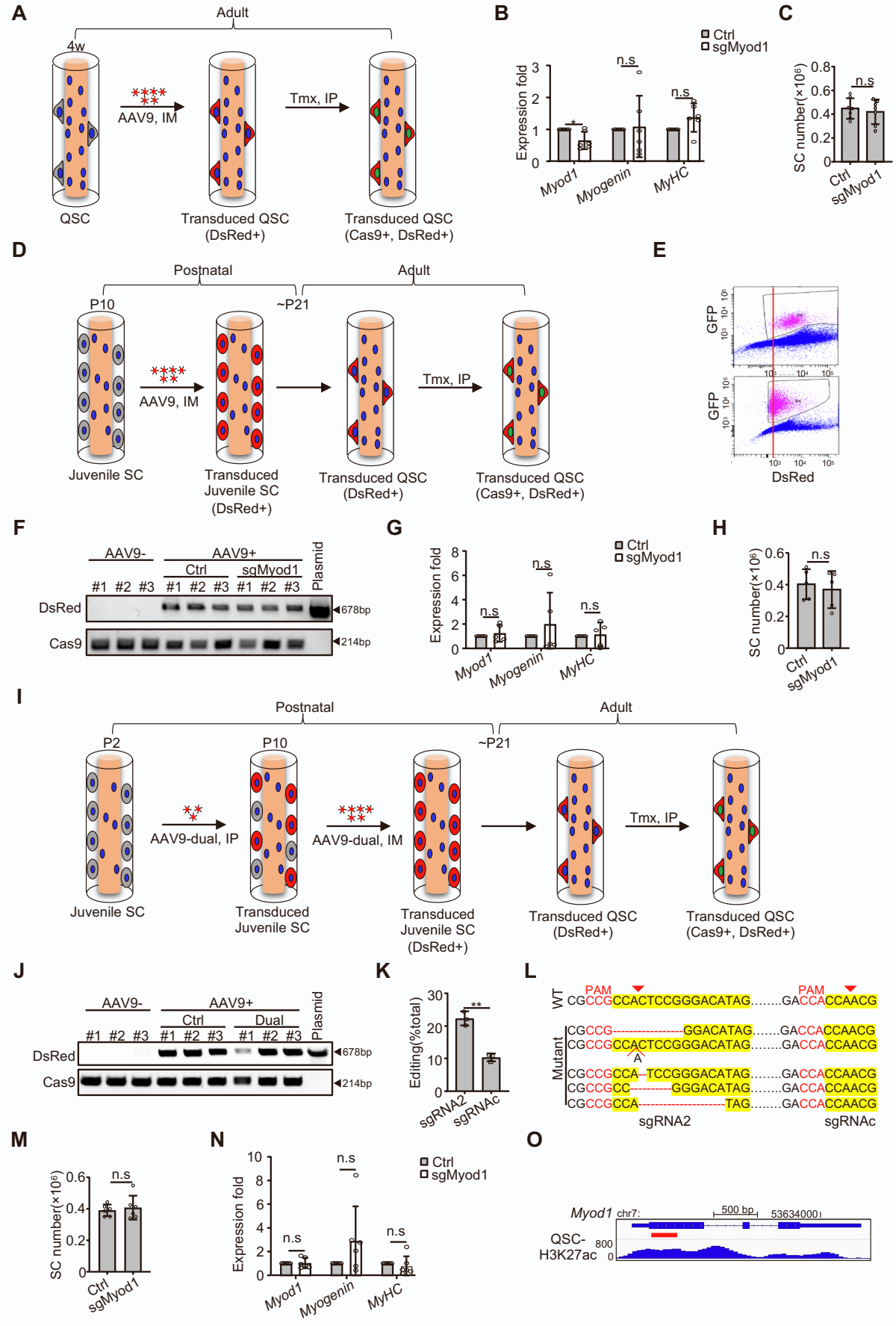
A
Adult
4w
AAV9, IM
Tmx, IP
QSC
Transduced QSC (DsRed+)
Transduced QSC (Cas9+, DsRed+)
B
Ctrl
sgMyod1
Expression fold
n.s
*
Myod1
Myogenin
MyHC
C
SC number(×10⁶)
n.s
Ctrl
sgMyod1
D
Postnatal
Adult
P10
~P21
AAV9, IM
Tmx, IP
Juvenile SC
Transduced Juvenile SC (DsRed+)
Transduced QSC (DsRed+)
Transduced QSC (Cas9+, DsRed+)
E
GFP
DsRed
F
AAV9-
AAV9+
Ctrl
sgMyod1
#1 #2 #3 #1 #2 #3 #1 #2 #3
Plasmid
DsRed
Cas9
678bp
214bp
G
Ctrl
sgMyod1
Expression fold
n.s
Myod1
Myogenin
MyHC
H
SC number(×10⁶)
n.s
Ctrl
sgMyod1
I
Postnatal
Adult
P2
P10
~P21
AAV9-dual, IP
AAV9-dual, IM
Tmx, IP
Juvenile SC
Transduced Juvenile SC
Transduced Juvenile SC (DsRed+)
Transduced QSC (DsRed+)
Transduced QSC (Cas9+, DsRed+)
J
AAV9-
AAV9+
Ctrl
Dual
#1 #2 #3 #1 #2 #3 #1 #2 #3
Plasmid
DsRed
Cas9
678bp
214bp
K
Editing(%total)
**
sgRNA2
sgRNAc
L
WT
PAM
PAM
CGCCGCCACTCCGGGACATAG.....GACCACCAACG
Mutant
CGCCG----------GGACATAG.....GACCACCAACG
CGCCGCCACTCCGGGACATAG.....GACCACCAACG
A
CGCCGCCA--TCCGGGACATAG.....GACCACCAACG
CGCCGCC---------GGGACATAG.....GACCACCAACG
CGCCGCCA----------TAG.....GACCACCAACG
sgRNA2
sgRNAc
M
SC number(×10⁶)
n.s
Ctrl
sgMyod1
N
Ctrl
sgMyod1
Expression fold
n.s
n.s
n.s
Myod1
Myogenin
MyHC
O
Myod1 chr7:
500 bp
53634000
QSC-H3K27ac
800
0

Figure S3. CRISPR/Cas9 fails to efficiently modify SCs at quiescent stage. Related to Figure 3. (**A**) Diagram to show the first strategy to edit QSCs. A high dose (5×10^{11} vg/mouse) of AAV9-sgMyod1 virus was intramuscularly (IM) injected into four-week-old *Pax7*$^{ER\text{-}Cas9}$ mice to transduce QSCs. Two weeks later, five consecutively intraperitoneal (IP) administrations of Tmx were conducted to induce Cas9 and GFP expression. The mice were sacrificed for SC isolation after another three weeks which provided enough time for possible editing. (**B**) Relative expressions of *Myod1*, *Myogenin* and *MyHC* mRNAs were detected in the SCs isolated from mice administrated in the first strategy (Figure 3B) and cultured for two days. n = 6 mice per group. (**C**) The number of SCs isolated from *Pax7*$^{ER\text{-}Cas9}$ mice in the first strategy. n = 7 mice per group. (**D**) Diagram to show the second strategy to edit QSCs. High dose of AAV9-sgMyod1virus was injected to *Pax7*$^{ER\text{-}Cas9}$ mice through IM at P10 to transduce proliferating juvenile SCs. Upon the termination of the postnatal myogenesis, a portion of the transduced cells were expected to become quiescence carrying the sgRNAs. Four weeks later, Tmx was injected via IP for five consecutive days to induce Cas9 and GFP expression and the mice were sacrificed for SC isolation and analysis after another three weeks. (**E**) Top: FACS plot showing the gating strategy to sort out Cas9-GFP positive SCs from *Pax7*$^{ER\text{-}Cas9}$ mice administrated in the second strategy (Figure 3G). A stronger DsRed signal compared to mice from Strategy 1 (bottom) indicates a higher transduction efficiency. (**F**) Genomic DNAs were isolated from FISCs of *Pax7*$^{ER\text{-}Cas9}$ mice in the second strategy and PCR was performed to amplify the DsRed or Cas9 coding region. Genomic DNAs from *Pax7*$^{ER\text{-}Cas9}$ mice without AAV9 administration were used as negative control and the AAV9-Myod1-sgRNA2 plasmid was used as positive control. n = 5 mice per group. (**G**) Relative expressions of *Myod1*, *Myogenin* and *MyHC* mRNAs were detected in the SCs isolated from the second strategy and cultured for two days. n = 5 mice per group. (**H**) The number of SCs isolated from *Pax7*$^{ER\text{-}Cas9}$ mice from the second strategy. n = 5 mice per group. (**I**) Diagram to show the third strategy to edit QSCs. A middle dose of AAV9-dual sgMyod1 virus was injected through IP into *Pax7*$^{ER\text{-}Cas9}$ mice at P2 and another high dose of the same virus was administrated at P10 through IM to transduce proliferating juvenile SCs, which was then followed by Tmx administration four weeks later to induce Cas9 and GFP expression. The mice were sacrificed for SC isolation after another three weeks. (**J**) Genomic DNAs were isolated from FISCs of *Pax7*$^{ER\text{-}Cas9}$ mice in the third strategy (Figure 3K) and PCR was performed to amplify the DsRed or Cas9 coding region. n = 6 mice per group. (**K**) Comparison of the editing efficiency between the sgRNA2 and sgRNAc sites. The editing efficiency at the two sites were markedly different (22.54% + 2.18% vs. 10.53% + 1.15%), possibly due to distinct accessibility to CRISPR/Cas9. n = 3 mice per group. (**L**) The five most frequently detected indel classes are shown with modifications occurring exclusively at the sgRNA2 target locus. (**M**) The number of SCs isolated from *Pax7*$^{ER\text{-}Cas9}$ mice in the third strategy. n = 6 mice per group. (**N**) Relative expressions of *Myod1*, *Myogenin* and *MyHC* mRNAs were detected in the above SCs cultured for four days. n = 6 mice per group. (**O**) Snapshot of H3K27ac ChIP-seq signal at *Myod1* locus in QSCs. The red bar indicates the targeted region. All qRT-PCR data were normalized to *18S* or *Gapdh* mRNA. All the bar graphs are presented as mean ± s.d. *P<0.05, **P<0.01. ns, no significance.

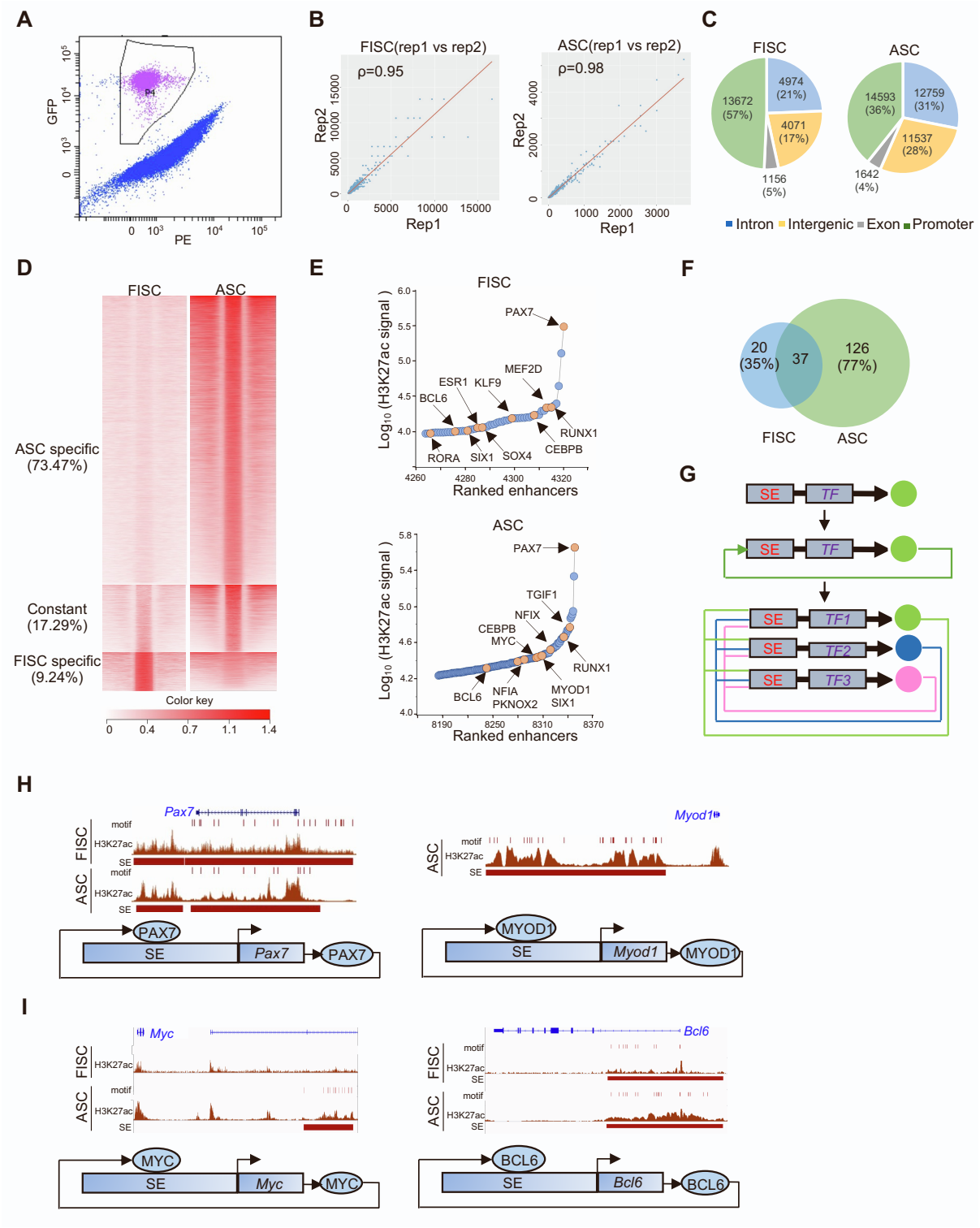

Figure S4. Key TFs regulating SC quiescence and activation are predicted through SEs. Related to Figure 4. (**A**) FACS plot showing the gating strategy for sorting out GFP positive SCs from *Pax7*-nGFP mice. (**B**) Reproducibility of two replicates of H3K27ac ChIP-seq datasets in FISCs or ASCs. (**C**) Genomic distribution of H3K27ac ChIP-seq reads in FISCs or ASCs. (**D**) Heatmaps of H3K27ac signals at ASC specific, constant, FISC specific enhancers. (**E**) Identification of SEs using ROSE in FISCs (Upper) and ASCs (Lower). Key TFs are shown. (**F**) Comparison of the SE landscapes between FISCs and ASCs. (**G**) Schematic illustration of the method to identify key TFs (Saint-André et

al., 2016). Cycles with various colors indicate different TFs. (**H**) Top: Genomic snapshots showing SEs associated with *Pax7* and *Myod1* loci. Bottom: illustration of auto-regulation of the above TFs and SEs. (**I**) Top: Genomic snapshots showing SEs associated with *Myc* and *Bcl6* loci. Bottom: illustration of auto-regulation of the above TFs and SEs.

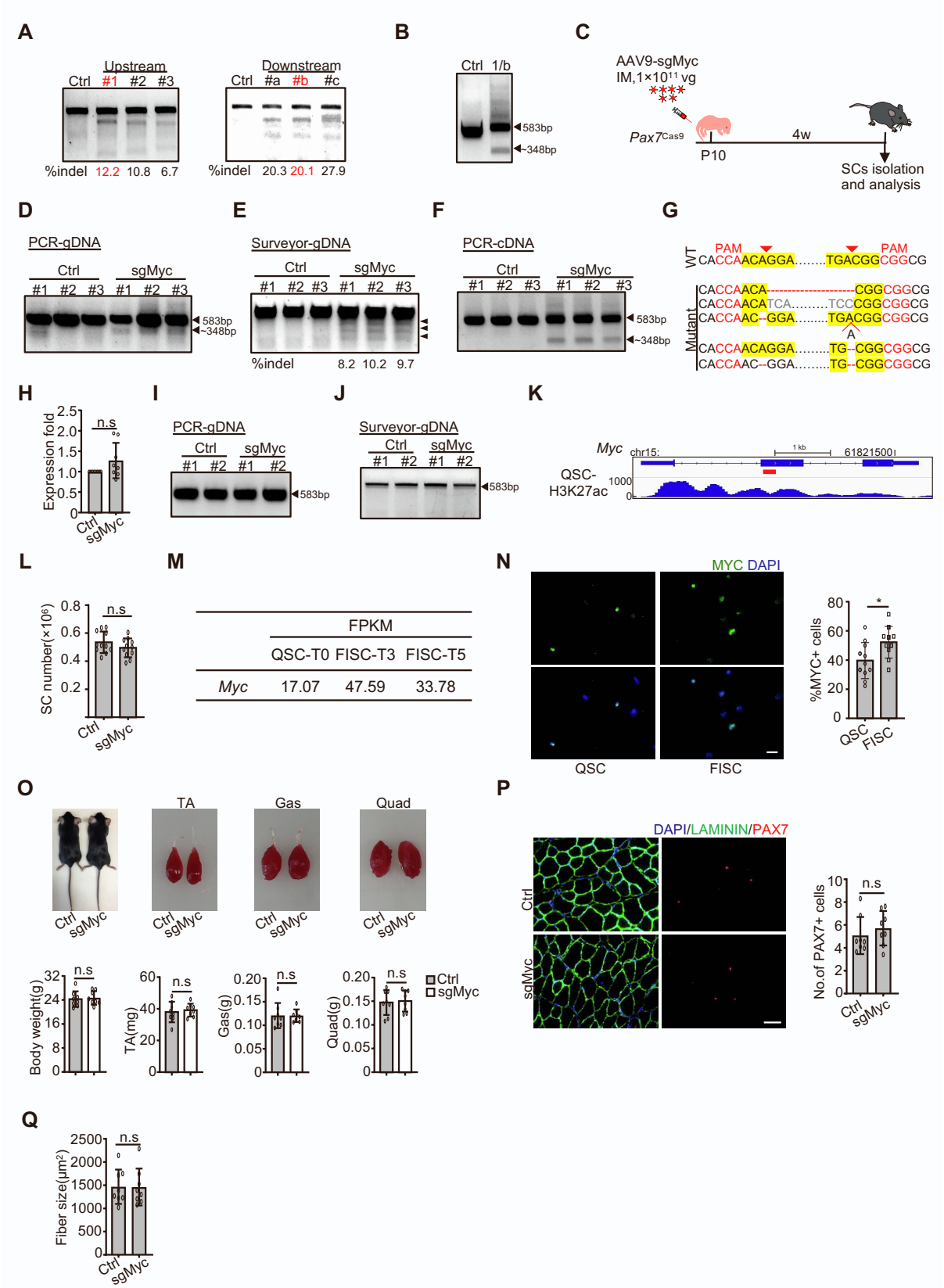

Figure S5. CRISPR/Cas9/AAV9-sgRNA mediated genome editing of *Myc* hinders SC activation and muscle regeneration. Related to Figure 5. (**A**) *In vitro* screening of sgRNAs targeting the up- and down-stream of *Myc* exon 2 in C2C12 cells. The frequency of indel occurrence is presented. SgRNA1 and sgRNAb which were expected to induce frameshift of *Myc* coding region were selected

for *in vivo* study and are marked in red. (**B**) Testing of the AAV9-dual sgMyc vector in C2C12 myoblasts. The above selected Myc-sgRNA1 and sgRNAb were cloned into the pAAV9-dual sgRNA vector sequentially and transfected into C2C12 cells together with a Cas9-expressing plasmid (pX458). Positively transfected cells were sorted out by GFP and DsRed one day after transfection and cultured for two days before PCR analysis to evaluate the deletion efficiency at *Myc* locus. Wild type (583 bp) and cleaved fragments (~348 bp) are indicated by arrowheads. (**C**) Schematic illustration of the experimental design for *in vivo* genome editing of *Myc* locus. *Pax7*^{Cas9} mice were intramuscularly administrated with middle dose of control or AAV9-dual sgMyc viruses at P10 and SCs were isolated four weeks later for analysis. **(D)** DNAs were isolated from the above FISCs and PCR was performed to test the cleavage efficiency. Wild type (583bp) and cleaved (~348bp) fragments are indicated by arrowheads. n = 3 mice per group. (**E**) The above genomic DNAs were subject to Surveyor assay to evaluate the editing efficiency at *Myc* locus. The arrowheads indicate the cleaved fragments by Surveyor. The frequency of indel occurrence is presented. n = 3 mice per group. (**F**) SCs isolated from *Pax7*^{Cas9} mice injected with high dose of AAV9-dual sgMyc viruses were cultured for 24 hrs and *Myc* cDNA was used for PCR analysis to test cleavage efficiency. Wild type (583bp) and cleaved (~348bp) fragments are indicated by arrowheads. (**G**) Representative sequencing reads for the AAV9-dual sgMyc targeted locus are shown. (**H**) The above SCs were cultured for 24 hrs and relative expression of *Myc* mRNAs was detected by qRT-PCR using *18S* mRNA as normalization. n = 8 mice per group. (**I**) The CRISPR/Cas9/AAV9-sgRNA system fails to modify *Myc* locus in QSCs. High dose of AAV9-dual sgMyc or control viruses were injected into *Pax7*$^{ER\text{-}Cas9}$ mice through IM at P10. Tamoxifen was injected intraperitoneally for five consecutive days to induce Cas9-GFP expression four weeks after AAV9 virus injection and the mice were sacrificed for SC isolation after another three weeks. Genomic DNAs from isolated SCs were subject to PCR analysis and a wild type band was amplified. n = 2 mice per group. (**J**) Surveyor nuclease assay was performed using the above DNA and no cleaved bands were detected. n = 2 mice per group. (**K**) Snapshot of H3K27ac ChIP-seq signal at *Myc* locus in QSCs. The red bar indicates the targeted region. (**L**) The number of SCs isolated from control or dual sgMyc virus treated mice. n = 11 mice per group. (**M**) Expression of *Myc* in QSCs or early activating FISCs was determined by RNA-seq (Machado et al., 2017). QSC-T0: SCs fixed by paraformaldehyde (PFA) before isolation. FISC-T3/5: SCs isolated by the standard 3 or 5-hour-long protocol. (**N**) IF staining of MYC in FISCs and QSCs (Left); the percentage of MYC positive cells was quantified from 11 randomly selected fields (Right). Scale bar, 20 μm. (**O**) *Pax7*^{Cas9} mice administrated with high dose of control or AAV9-dual sgMyc viruses did not show alteration in the weight of whole body or limb muscles. n = 8 mice per group. Representative images of mice and muscles are shown in the top. (**P**) Left: Immunostaining of PAX7 (red) and LAMININ (green) was performed on the uninjured TA muscle. Right: The number of PAX7 positive cells per 100 fibers was counted. n = 8 mice per group. For each mouse, an average of 17 randomly selected fields were quantified. (**Q**) Average fiber size of the uninjured TA muscle was quantified. n = 8 mice per group. Scale bar, 50 μm. All the bar graphs are presented as mean ± s.d. *P<0.05. ns, no significance.

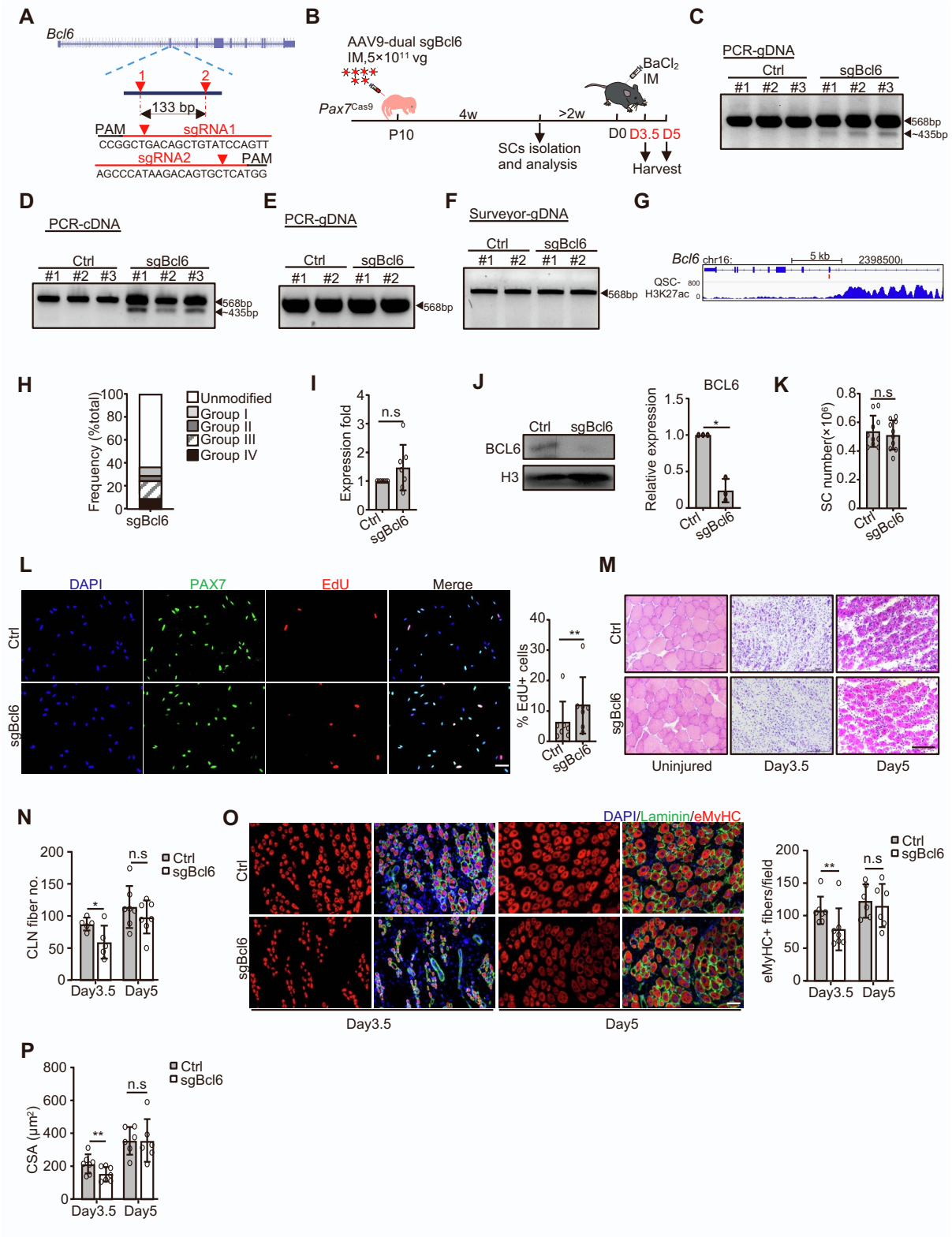

Figure S6. CRISPR/Cas9/AAV9-sgRNA mediated genome editing of *Bcl6* leads to abnormality of SC activation and muscle regeneration. Related to Figure 5. (**A**) Design of dual sgRNAs targeting *Bcl6* locus. SgRNA1 and sgRNA2 were designed to delete a 133 bp of exon 3. (**B**) Schematic illustration of the experimental design for *in vivo* genome editing of *Bcl6* locus followed by analysis of its effect on SCs and muscle regeneration. *Pax7*^{Cas9} mice were intramuscularly administrated with high dose of control or AAV9-dual sgBcl6 virus at P10 and SCs were isolated four weeks later for analyses.

To assay for muscle regeneration, $BaCl_2$ was intramuscularly injected into TA muscle at least six weeks after AAV9 virus administration (D0). The injected muscle was harvested 3.5 (D3.5) or 5 days (D5) post injury and subject to analysis. (**C**) Genomic DNAs were isolated from the above sorted SCs and PCR analysis was performed to test the cleavage efficiency. Wild type (568 bp) and cleaved (~435 bp) fragments are indicated by arrowheads. (**D**) SCs isolated from *Pax7*^{Cas9} mice injected with high dose of AAV9-dual sgBcl6 viruses were cultured for 24 hrs and Bcl6 cDNAs were used for PCR analysis to test cleavage efficiency. Wild type (568bp) and cleaved (~435bp) fragments are shown by arrowheads. (**E**) The CRISPR/Cas9/AAV9-sgRNA system fails to modify *Bcl6* locus in QSCs. High dose of AAV9-dual sgBcl6 or control viruses were injected into *Pax7*$^{ER\text{-}Cas9}$ mice through IM at P10. Tamoxifen was injected intraperitoneally for five consecutive days to induce Cas9-GFP expression four weeks after AAV9 virus injection and the mice were sacrificed for SC isolation after another three weeks. Genomic DNAs from isolated SCs were subject to PCR analysis and a wild type band was amplified. n = 2 mice per group. (**F**) Surveyor nuclease assay was performed using the above DNAs and no cleaved bands were detected. n = 2 mice per group. (**G**) Snapshot of H3K27ac ChIP-seq signal at *Bcl6* locus in QSCs. The red bar indicates the targeted region. (**H**) Distribution of the total sequencing reads for the AAV9-dual sgBcl6 targeted locus. Group I-IV were defined according to Figure S2N. (**I**) The above SCs were cultured for 24 hrs and relative expression of *Bcl6* mRNAs was detected by qRT-PCR. The qRT-PCR data were normalized to *18S* mRNA. n = 7 mice per group. (**J**) BCL6 protein level in the above SCs was examined by Western blot (Left) and the band intensity was quantified by Image J (Right). Histone H3 was used as loading control. n = 3 mice per group. (**K**) The number of SCs isolated from the above control or dual sgBcl6 virus treated mice. n = 10 mice per group. (**L**) The above FISCs were labeled with EdU for 24 hrs and the percentage of EdU positive cells was quantified. n = 7 mice per group. For each mouse, an average of 26 randomly selected fields were quantified. Scale bar, 50 μm. (**M-N**) H&E staining was performed 3.5 (D3.5) or 5 days (D5) post $BaCl_2$ injection (M) and the regenerating myofibers with CLN per field was quantified (N). n = 5 to 7 mice per group. For each mouse, an average of 6 randomly selected fields were quantified. Scale bar, 100 μm. (**O**) Immunostaining of eMyHC (red) and LAMININ (green) on the above TA muscle sections (Left) and the number of eMyHC+ myofibers was counted (Right). n = 6 to 7 mice per group. For each mouse, an average of 6 randomly selected fields were quantified. Scale bar, 50 μm. (**P**) The cross-sectional area (CSA) of the newly formed fibers with CLN was quantified. n = 6 to 7 mice per group. All the bar graphs are presented as mean ± s.d. *P<0.05, **P<0.01. ns, no significance.

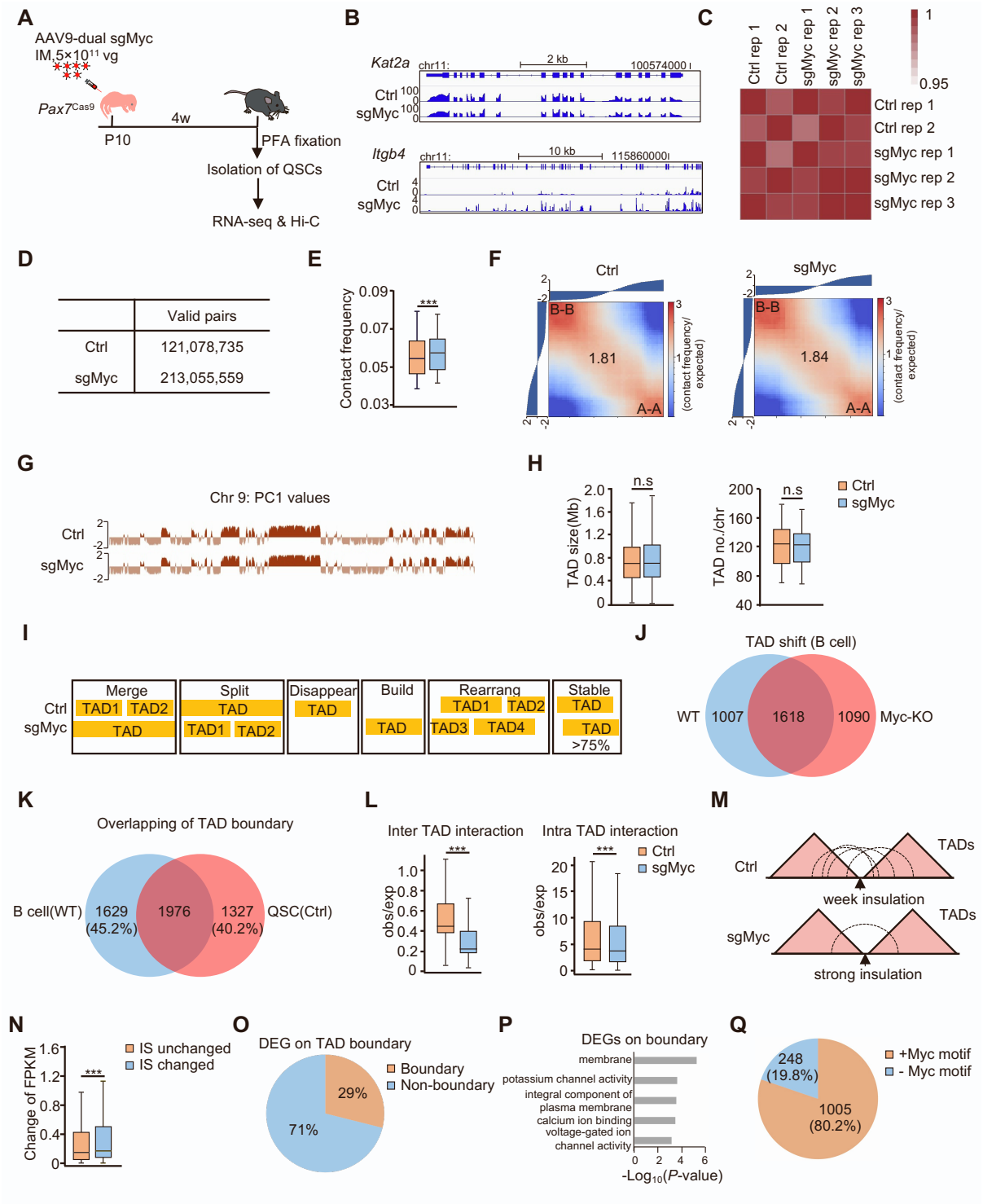

Figure S7. MYC orchestrates SC activation through impinging on 3D chromatin architecture. Related to Figure 6. (**A**) Schematic illustration of the experimental design to isolate Myc deficient QSCs for RNA-seq and Hi-C. *Pax7*^{Cas9} mice were intramuscularly administrated with high dose of control or AAV9-dual sgMyc viruses at P10 and SCs were isolated four weeks later. QSCs were isolated according to published protocol (Machado et al., 2017) using prior PFA fixation then subjected to RNA-seq and Hi-C experiment. (**B**) Genomic snapshots showing the expression of two known MYC regulated genes, *Kat2a* and *Itgb4*, in sgMyc vs. Ctrl. (**C**) Heatmap showing correlation between different groups and replicates (two biological replicates for control and three biological replicates for

sgMyc group) of the Hi-C experiments. (**D**) The number of valid pairs generated from Hi-C in each group. (**E**) Normalized interaction frequency for long-rang interactions (>5×10^{11} bp) in Ctrl and sgMyc QSCs**.** (**F**) Average contact frequency enrichment showing the extent of compartmentalization in Ctrl (Left) and sgMyc (Right) QSCs. (**G**) Distributions of PC1 values across entirety of chromosome 9 in Ctrl and sgMyc QSCs. The A compartments are shown in puce, and the B compartments are shown in beige. (**H**) Average TAD size (Left) and the number of TADs per chromosome (Right) in each group. (**I**) Illustration of TAD shift (Ke et al., 2017). If the overlapped portion of a given TAD in Ctrl and sgMyc group was over 0.75, it was defined as stable TAD, otherwise it was called rearranged TAD. If two or more TADs fused into one or on the contrary one divided into two or more TADs upon MYC depletion, the changes were named “merge” or “split” respectively. If one TAD was only identified in Ctrl or sgMyc QSCs, the changes were defined as “disappear” or “build”. TAD shift was defined when a TAD was split, merged, disappeared, built or rearranged upon MYC depletion. (**J**) Venn diagram showing the number of shifted TADs in WT vs Myc-KO B cells (Kieffer-Kwon et al., 2017). (**K**) Venn diagram showing the overlap of the TAD boundaries identified in WT B cells and Ctrl QSCs. (**L**) Boxplots showing inter- (Left) or intra-TAD (Right) interactions in Ctrl and sgMyc QSCs. Obs: observed; exp: expected. (**M**) Illustration of the change of IS upon MYC deletion (Stadhouders et al., 2018). (**N**) Boxplot showing the absolute FPKM changes for genes located within boundaries with at least 20% IS value change upon Myc depletion compared with those residing in IS unchanged boundaries. (**O**) Pie chart showing genomic distribution of DEGs within TAD boundary and non-boundary regions. (**P**) GO analysis of the DEGs resided within the boundaries was performed and the top five enriched items are shown in y axis. (**Q**) Pie chart showing the portion of TAD boundary located H3K27ac peaks containing MYC motif. Statistical analyses in **E**, **H**, **L** and **N** were done by Wilcoxon rank-sum test; ***P<0.001. ns, no significance.

Supplemental Experimental Procedures

Mice. *Pax7*-nGFP, *Pax7*^{Cre} and *Pax7*^{CreER} mice were kindly provided by Dr. Zhenguo Wu (Hong Kong University of Science & Technology). The Cre dependent *Rosa26*$^{Cas9\text{-}EGFP}$ knockin mice (B6;129-Gt (ROSA)26Sor$^{tm1(CAG\text{-}cas9*\text{-}EGFP)\ Fezh/J}$; stock number 024857) were obtained from the Jackson Laboratory. To generate Cas9 knockin mice, homozygous *Pax7*^{Cre} or *Pax7*^{CreER} mice were crossed with Rosa26$^{Cas9\text{-}EGFP}$ mice. For inducible Cas9 expression, Tamoxifen (100 mg/Kg body weight) was injected intraperitoneally into *Pax7*$^{ER\text{-}Cas9}$ mice for five consecutive days. Each mouse strain was genotyped by PCR using DNA extracted from mouse tail tissues. To induce acute injury, over 8-week-old mice were injected with 50 µL of 1.2% $BaCl_2$ (w/v in H_2O) solution into the tibialis anterior (TA) muscle. TA muscles were harvested at designated time points for further analysis. Primers used for genotyping are listed in Table S7.

Plasmids. To construct the AAV9-sgRNA transfer plasmids, the AAV: ITR-U6-sgRNA (backbone)-pCBh-Cre-WPRE-hGHpA-ITR (Addgene, 60229) was used as donor plasmid. Coding sequencing for DsRed was PCR-amplified and cloned into the donor plasmid through replacing the sequence encoding Cre using Age I and EcoR I sites. The CBh promoter was substituted with CMV promoter to drive DsRed expression. For single sgRNA expression system, sgRNA with the highest editing efficiency assessed by Surveyor nuclease assay was inserted into the AAV9-sgRNA vector (AAV: ITR-U6-sgRNA(backbone)-CMV-DsRed-WPRE- hGHpA-ITR) using Sap I site. To generate dual AAV-sgRNAs expression plasmid, the second sgRNA with good editing efficiency and targeting about 100 bp-300 bp away from the first sgRNA was constructed into the AAV9-sgRNA vector together with the gRNA cassette and U6 promoter using Xba I and Kpn I sites. To increase the editing efficiency, the two selected sgRNAs were designed to target 5' end of the coding region and the predicted deletion should cause frameshift of target gene. Primers for AAV9-sgRNA vector construction are listed in Table S7.

Cell culture. Mouse C2C12 myoblast cells (CRL-1772) and human HEK293FT cells were obtained from ATCC and cultured in DMEM with 10% FBS, 100 units/ml penicillin, 100 µg/ml streptomycin and 2 mM L-glutamine (GM, growth medium) in 5% CO_2 at 37 ◦C.

Satellite cell isolation, culture and EdU incorporation assay. Isolated satellite cells were cultured in growth medium (F10 medium (Merck Millipore) supplemented with 20% FBS, 1% penicillin/streptomycin and 5 ng/mL basic fibroblast growth factor (bFGF)) at 37◦C in 5% CO_2. To induce spontaneous differentiation, satellite cells were cultured in growth medium up to four days. For EdU incorporation assay, EdU was added to the SC culture medium with a final concentration of 10 mM and the incorporation assay was detected by Click-iT EdU kit (Invitrogen) according to the manufacturer's instructions.

SgRNA design, selection and Surveyor nuclease assay. In brief, site specific sgRNAs were predicted following a web tool Crispor (Haeussler et al., 2016) (http://crispor.tefor.net/). To minimize off-target effects, only sgRNAs with a score higher than 5 were selected. To determine the editing efficiency, annealed oligonucleotides were constructed into a Cas9-EGFP expressing vector (pX458, Addgene) using Bbs I site. SgRNA-pX458 plasmids were transiently transfected into C2C12 using

Lipofectamine 3000. GFP positive cells were sorted out using FACS 48 hrs after transfection and cultured for another two days. Genomic DNAs were extracted by QuickExtract (Epicentre) solution and amplified by Phusion High-Fidelity DNA Polymerase (NEB) using primers against the edited locus. Purified PCR products were subject to Surveyor nuclease assay (Integrated DNA Technologies) according to the manufacturer's protocol (Ran et al., 2013). Briefly, 360 ng of DNA was denatured at 95°C and re-annealed to form hetero-duplexes. The resulting product was digested by Surveyor Nuclease S at 42 °C for 30 minutes and separated on a 2% agarose gel. The percentage of indel formation was determined by relative band intensities. The band intensity of the gel was first evaluated by Image J. The percentage of the PCR product cleaved (f_{cut}) for each lane was then calculated using the formula: f_{cut} = (b + c)/ (a + b + c), where a is the integrated intensity of the undigested PCR product and b and c are the integrated intensities of each cleavage product. The percentage of indel was then estimated by the formula: indel (%) = 100 × (1-$\sqrt{(1-fcut)}$). For the control group, genomic DNA from C2C12 cells transfected with Cas9-EGFP expressing plasmid (pX458) without any sgRNA insertion was used and subjected to Surveyor nuclear assay. Sequences for sgRNAs and primers used for Surveyor assay are listed in Table S7.

AAV9 virus production, purification and injection. AAV9 serotype plasmid and pDF6 are kind gifts from Dr. Bin Zhou (Yu et al., 2016). AAV9 virus particles were produced in HEK293FT cells by the triple transfection method (Grieger et al., 2006). In brief, HEK293FT cells were seeded in T75 flask and transiently transfected with AAV9-sgRNA vector (5 μg), AAV9 serotype plasmid (5 μg), and pDF6 (AAV helper plasmid) (10 μg) at a ratio of 1:1:2 using polyethyleneimine (PEI) when the cell reached 80%~90% confluent. Twenty-four hrs after transfection, the cells were changed to growth medium (DMEM with 10% FBS, 100 units/ml penicillin, 100 μg/ml streptomycin and 2 mM L-glutamine) and cultured for another forty-eight hrs. The cells were harvested by Trypsin-EDTA (Gibco) and washed with PBS for two times. To release the AAV9 virus, the pellet was re-suspended with lysis buffer (Tris-HCl, PH 8.0, 50 mM; NaCl, 150 mM) followed by three sequential freeze–thaw cycles (liquid nitrogen/37°C). The lysate was treated with Benzonase (Sigma) together with $MgCl_2$ (final concentration: 1.6 mM) at 37°C for 0.5~1 hr followed by centrifugation at 3,000 rpm for 10 minutes. The supernatant was filtered with 0.45 μm sterile filter and added with equal volume of 1 M NaCl and 20% PEG8000 (w/v) to precipitate the virus at 4 °C overnight. After centrifugation at 12,000 g for 30 minutes at 4 °C, the supernatant was remove and the pellet was re-suspended with sterile PBS and then subject to centrifugation at 3,000 g for 10 minutes. Equal volume of chloroform was then added and shaken. The mixture was spun down at 12,000 g for 15 minutes at 4 °C. The aqueous layer was filtered by 0.22 μm sterile filter and passed through a 100 kDa MWCO (Millipore). The concentrated solution was washed with sterile PBS for three times. The tilter of the AAV9 virus was determined by qRT-PCR using primers targeting the CMV promoter. For AAV9 administration, 50-100 μL of AAV9-sgRNA (high dose: 5×10^{11} vg; middle dose: 1×10^{11} vg; low dose: 0.2×10^{11} vg) or control (AAV9-sgRNA vector without sgRNAs insertion) virus was diluted in saline and injected systemically through intraperitoneal (IP) injection on postnatal day 2 (P2) or locally to the skeletal muscles through intramuscular (IM) injection on P10. All the used primers are listed in Table S7.

Immunoblotting, immunostaining and immunohistochemistry. Tissue samples were homogenized in 400 μl of ice cold RIPA buffer supplemented with protease inhibitors cocktail (Sigma-Aldrich) and lysed on ice for 40 minutes. Total cell extracts for Western blot were prepared as described previously

(Lu et al., 2013; Zhou et al., 2015). Following antibodies were used: MYOD1 (Dako, M3512, 1:2000), α-TUBULIN (Santa Cruz Biotechnology, sc-23948, 1:2000), Cas9 (Cell Signaling Technology, #14697, 1:1000), PAX7 (Developmental Studies Hybridoma Bank; 1:1000), GFP (Santa Cruz Biotechnology, sc-8334, 1:1000), GAPDH (Santa Cruz Biotechnology, sc-137179, 1:2000), Histone H3 (Santa Cruz Biotechnology, sc-517576, 1:3000), MYC (Santa Cruz Biotechnology, sc-40, 1:1000), BCL6 (Santa Cruz Biotechnology, sc-365618/sc-7388, 1:500), MYOGENIN (Santa Cruz Biotechnology, sc-576, 1:1000). For immunofluorescence staining, following antibodies and related dilutions were used: MYOD1 (Dako, M3512, 1:800), PAX7 (Developmental Studies Hybridoma Bank; 1:100), DsRed (Santa Cruz Biotechnology, sc-390909, 1:400), MYC (Santa Cruz Biotechnology, sc-40, 1:500). Hematoxylin and eosin (H&E) staining on frozen muscle sections was performed as described previously (Diao et al., 2012). Immunofluorescence staining on frozen muscle sections was performed using the following antibodies: Laminin (Sigma, L9393, 1:800), eMyHC (Sigma, 1:200), PAX7 (Developmental Studies Hybridoma Bank; 1:50). All fluorescent images were captured with a fluorescence microscope (Leica DM6000B).

qRT-PCR. Total RNAs from cells were extracted using TRIzol reagent (Life Technologies) according to the manufacturer's instructions and cDNAs were prepared using PrimeScript™ RT Master Mix kit (Takara, RR036A). Analysis of mRNA expression was performed with SYBR Green Master Mix (Life Technologies) on a 7900HT System (Life Technologies). All the used primers are listed in Table S7.

RNA-seq and data analysis. RNA-seq was performed as described previously (Zhao et al., 2019). Total RNAs were extracted from PFA fixated, freshly isolated or cultured SCs and subject to poly(A) selection (Ambion, 61006) followed by library preparation using NEBNext® Ultra™ II RNA Library Preparation Kit (NEB). Libraries with barcodes were pooled at equal concentrations and sequenced on the Illumina HiSeq 1500 platform. For data analysis, sequenced reads were mapped to reference mouse genome using TopHat (v2.0.13). Cufflinks (v2.1.1) was then employed to estimate transcript abundance. Abundance was reported in Fragments Per Kilobase per Million (FPKM). Differentially expressed genes were identified if the change of expression level exceeds a fold change threshold (> 2).

ChIP-seq and data analysis. ChIP-seq and the data analysis were performed following the procedures described in our previous studies (Chen et al., 2019; Peng et al., 2017). In brief, chromatins from freshly isolated or cultured SCs were fragmented using sonicator and incubated with 5 μg antibody against histone H3-K27 acetylation (Abcam, ab4729, rabbit poly-clonal) overnight at 4 °C. The purified DNA (200 ng) was subject to library preparation using NEBNext® Ultra™ II DNA Library Preparation Kit (NEB). Libraries with barcodes were pooled and sequenced on the Illumina HiSeq 1500 platform. For data analysis, a standard approach was used to conduct base calling and convert the results into raw reads in FASTQ format. After adapter trimming and quality filtering, reads were first aligned to mm9 reference genome by Bowtie2 with default parameters, then removed duplication and called enriched regions (peaks) by MACS2 with q-value equal to 0.01. Annotation of enhancers and super enhancers was performed as described before with minor adjustment (Peng et al., 2017). Enriched H3K27ac regions(peaks) were identified by MACS2 using merged bam files from all replicates at each stage with q-value 0.01. Peaks were subject to a filter to exclude the ENCODE blacklisted regions as well as those within +/-2 kb of a Refseq Transcription Start Site (TSS) and the

filtered peaks were defined as enhancers. For super enhancer identification, unlike ROSE (Whyte et al., 2013) pipeline in which enhancers within 12.5 kb of each other are combined into stitched enhancer regions and then assigned to nearby genes, in our prediction, enhancers were first assigned to expressed genes (RPKM >0.5) whose TSSs are nearest to the center of the enhancer region; then the enhancers assigned to the same genes and within 12.5 kb of one another were stitched together and further subject to super enhancer identification using the ROSE algorithm. SE constituents were extended by 500 bp on both side and used as input regions to scan motifs for transcription factors by FIMO with default parameters. The Position weight matrix (PWM) of the motifs were obtained from the TRANSFAC database. For key TF prediction, if its DNA binding motif was predicted in its own SE region for at least three times, this kind of SE associated TFs was assigned as auto-regulated TFs; key TFs were defined as auto-regulated TFs whose binding motifs were predicted in the SE regions of other auto-regulated TFs.

Hi-C and data analysis. The *in situ* Hi-C libraries were prepared as previously reported (Ke et al., 2017; Rao et al., 2014; Stadhouders et al., 2018). Briefly, isolated SCs were digested using 100U DpnII overnight at 37 °C and then filled in with biotin for 1.5 hours at 37 °C; ligated for 4.5 hours at room temperature. DNA was purified by ethanol precipitation, and then sheared into 300-400bp fragments using Covaris S220. DNA fragments containing biotin were enriched by Dynabeads MyOne Streptavidin C1 (Invitrogen 65001) for 15 min at room temperature, followed by end repairing, adaptor ligation and PCR amplification as described (Rao et al., 2014). At least two biological replicates were performed for both control and sgMyc groups. The libraries were then sequenced via the Illumina HiSeq X Ten system at Genewiz company.

The *in-situ* Hi-C data was processed following a standard pipeline Hi-C-Pro (Servant et al., 2015). Briefly, the reads were aligned to reference genome (mm9) in two steps: global alignment was first performed for all pair-end reads; unaligned reads were then trimmed by restriction enzyme and aligned again. All aligned reads were then merged together to assign to restriction fragments. In this step, invalid fragments (dangling end, self-cycle etc.) were discarded and PCR duplications were removed for each biological replicate separately. At last, all validate pairs were normalized by read depth using HOMER (Heinz et al., 2010) followed by ICE matrix balancing (Imakaev et al., 2012) to further get interaction matrix.

To separate the genome into A/B compartments, ICE normalized Hi-C matrices at 100-kb resolution were split into chromosomal matrices and Pearson correlation was applied in the transformed correlation matrices. The annotation of genes including the expression profile was used to assign negative and positive PC1 categories to each compartment. The compartmentalization strength was measured using cool tools (https://github.com/mirnylab/cooltools). Basically, all compartment bins were divided into 50 degrees based on the ranking of PC1 value, and then the average interaction strength (observed/expected) between each degree was calculated to obtain the saddle plot. The compartmentalization score was calculated using top 20% of intra-compartment divided by top 20% of inter-compartment based on PC1 value.

TopDom (Shin et al., 2016) was applied to identify TADs. Briefly, TopDom first computed a score by calculating the average interaction frequency around a distinct window of each bin and then identified TAD boundary under statistical testing as the local minimal signal within certain distance. Normalized contact matrices at 40 kb resolution were used for TAD identification. The unaltered TADs were defined following two criteria: 1) The distance of both TAD boundaries between two conditions

was less than or equal to 40 kb; 2) The overlapping between two TADs should be larger than 75% to exclude TADs with small size. The insulation index for each bin was generated based on a previously described method (Crane et al., 2015) by calculating the number of interactions across a specific bin on each side. The insulation score of the identified TAD border was defined through the same method (Crane et al., 2015), which used the local maximum on the outside of TAD to minus the local minimum of the inside of TAD of each boundary bin.

Deep-seq. Deep-seq was performed as previously described (Guo et al., 2018, 2017; Johansen et al., 2017). Briefly, genomic DNAs from AAV9-sgRNA infected SCs were amplified using Q5 High-Fidelity 2× Master Mix (NEB). PCR products were purified through QIAQuick PCR purification kit (Qiagen) and subject to library preparation using NEBNext® Ultra™ II DNA Library Preparation Kit (NEB). Libraries with barcodes were pooled and sequenced on the Illumina HiSeq 1500 platform. For data analysis, an online tool CRISPResso2 (http://crispresso.pinellolab.partners.org/) (Clement et al., 2019) was employed to calculate the indel occurrence. Primers used for Deep-seq are listed in Table S7.

Supplemental References

Chen, F., Zhou, J., Li, Y., Zhao, Y., Yuan, J., Cao, Y., Wang, L., Zhang, Z., Zhang, B., Wang, C.C., et al. (2019). YY1 regulates skeletal muscle regeneration through controlling metabolic reprogramming of satellite cells. The EMBO Journal *38*, e99727.

Clement, K., Rees, H., Canver, M.C., Gehrke, J.M., Farouni, R., Hsu, J.Y., Cole, M.A., Liu, D.R., Joung, J.K., Bauer, D.E., et al. (2019). CRISPResso2 provides accurate and rapid genome editing sequence analysis. Nature Biotechnology *37*, 224–226.

Crane, E., Bian, Q., McCord, R.P., Lajoie, B.R., Wheeler, B.S., Ralston, E.J., Uzawa, S., Dekker, J., and Meyer, B.J. (2015). Condensin-driven remodelling of X chromosome topology during dosage compensation. Nature *523*, 240–244.

Diao, Y., Guo, X., Li, Y., Sun, K., Lu, L., Jiang, L., Fu, X., Zhu, H., Sun, H., Wang, H., et al. (2012). Pax3/7BP Is a Pax7- and Pax3-Binding Protein that Regulates the Proliferation of Muscle Precursor Cells by an Epigenetic Mechanism. Cell Stem Cell *11*, 231–241.

Grieger, J.C., Choi, V.W., and Samulski, R.J. (2006). Production and characterization of adeno-associated viral vectors. Nature Protocols *1*, 1412–1428.

Guo, T., Feng, Y.-L., Xiao, J.-J., Liu, Q., Sun, X.-N., Xiang, J.-F., Kong, N., Liu, S.-C., Chen, G.-Q., Wang, Y., et al. (2018). Harnessing accurate non-homologous end joining for efficient precise deletion in CRISPR/Cas9-mediated genome editing. Genome Biology *19*, 170.

Guo, Y., VanDusen, N.J., Zhang, L., Gu, W., Sethi, I., Guatimosim, S., Ma, Q., Jardin, B.D., Ai, Y., and Zhang, D. (2017). Analysis of cardiac myocyte maturation using CASAAV, a platform for rapid dissection of cardiac myocyte gene function in vivo. Circulation Research *120*, 1874–1888.

Haeussler, M., Schönig, K., Eckert, H., Eschstruth, A., Mianné, J., Renaud, J.-B., Schneider-Maunoury, S., Shkumatava, A., Teboul, L., and Kent, J. (2016). Evaluation of off-target and on-target scoring algorithms and integration into the guide RNA selection tool CRISPOR. Genome Biology *17*, 148.

Heinz, S., Benner, C., Spann, N., Bertolino, E., Lin, Y.C., Laslo, P., Cheng, J.X., Murre, C., Singh, H., and Glass, C.K. (2010). Simple Combinations of Lineage-Determining Transcription Factors Prime cis-Regulatory Elements Required for Macrophage and B Cell Identities. Molecular Cell *38*, 576–589.

Imakaev, M., Fudenberg, G., McCord, R.P., Naumova, N., Goloborodko, A., Lajoie, B.R., Dekker, J., and Mirny, L.A. (2012). Iterative correction of Hi-C data reveals hallmarks of chromosome organization. Nature Methods *9*, 999–1003.

Johansen, A.K., Molenaar, B., Versteeg, D., Leitoguinho, A.R., Demkes, C., Spanjaard, B., de Ruiter, H., Akbari Moqadam, F., Kooijman, L., and Zentilin, L. (2017). Postnatal cardiac gene editing using CRISPR/Cas9 with AAV9-mediated delivery of short guide RNAs results in mosaic gene disruption. Circulation Research *121*, 1168–1181.

Ke, Y., Xu, Y., Chen, X., Feng, S., Liu, Z., Sun, Y., Yao, X., Li, F., Zhu, W., and Gao, L. (2017). 3D chromatin structures of mature gametes and structural reprogramming during mammalian embryogenesis. Cell *170*, 367-381. e20.

Kieffer-Kwon, K.-R., Nimura, K., Rao, S.S.P., Xu, J., Jung, S., Pekowska, A., Dose, M., Stevens, E., Mathe, E., Dong, P., et al. (2017). Myc Regulates Chromatin Decompaction and Nuclear Architecture during B Cell Activation. Molecular Cell *67*, 566-578.e10.

Lu, L., Sun, K., Chen, X., Zhao, Y., Wang, L., Zhou, L., Sun, H., and Wang, H. (2013). Genome-wide survey by ChIP-seq reveals YY1 regulation of lincRNAs in skeletal myogenesis. The EMBO Journal *32*, 2575–2588.

Machado, L., de Lima, J.E., Fabre, O., Proux, C., Legendre, R., Szegedi, A., Varet, H., Ingerslev, L.R., Barrès, R., and Relaix, F. (2017). In situ fixation redefines quiescence and early activation of skeletal muscle stem cells. Cell Reports *21*, 1982–1993.

van Overbeek, M., Capurso, D., Carter, M.M., Thompson, M.S., Frias, E., Russ, C., Reece-Hoyes, J.S., Nye, C., Gradia, S., and Vidal, B. (2016). DNA repair profiling reveals nonrandom outcomes at Cas9-mediated breaks. Molecular Cell *63*, 633–646.

Peng, X.L., So, K.K., He, L., Zhao, Y., Zhou, J., Li, Y., Yao, M., Xu, B., Zhang, S., and Yao, H. (2017). MyoD-and FoxO3-mediated hotspot interaction orchestrates super-enhancer activity during myogenic differentiation. Nucleic Acids Research *45*, 8785–8805.

Ran, F.A., Hsu, P.D., Wright, J., Agarwala, V., Scott, D.A., and Zhang, F. (2013). Genome engineering using the CRISPR-Cas9 system. Nature Protocols *8*, 2281–2308.

Rao, S.S.P., Huntley, M.H., Durand, N.C., Stamenova, E.K., Bochkov, I.D., Robinson, J.T., Sanborn, A.L., Machol, I., Omer, A.D., Lander, E.S., et al. (2014). A 3D Map of the Human Genome at Kilobase Resolution Reveals Principles of Chromatin Looping. Cell *159*, 1665–1680.

Saint-André, V., Federation, A.J., Lin, C.Y., Abraham, B.J., Reddy, J., Lee, T.I., Bradner, J.E., and Young, R.A. (2016). Models of human core transcriptional regulatory circuitries. Genome Res. *26*, 385–396.

Servant, N., Varoquaux, N., Lajoie, B.R., Viara, E., Chen, C.-J., Vert, J.-P., Heard, E., Dekker, J., and Barillot, E. (2015). HiC-Pro: an optimized and flexible pipeline for Hi-C data processing. Genome Biol *16*, 259.

Shin, H., Shi, Y., Dai, C., Tjong, H., Gong, K., Alber, F., and Zhou, X.J. (2016). TopDom: an efficient and deterministic method for identifying topological domains in genomes. Nucleic Acids Res *44*, e70–e70.

Stadhouders, R., Vidal, E., Serra, F., Di Stefano, B., Le Dily, F., Quilez, J., Gomez, A., Collombet, S., Berenguer, C., Cuartero, Y., et al. (2018). Transcription factors orchestrate dynamic interplay between genome topology and gene regulation during cell reprogramming. Nature Genetics *50*, 238–249.

Whyte, W.A., Orlando, D.A., Hnisz, D., Abraham, B.J., Lin, C.Y., Kagey, M.H., Rahl, P.B., Lee, T.I., and Young, R.A. (2013). Master transcription factors and mediator establish super-enhancers at key cell identity genes. Cell *153*, 307–319.

Yu, W., Huang, X., Tian, X., Zhang, H., He, L., Wang, Y., Nie, Y., Hu, S., Lin, Z., Zhou, B., et al. (2016). GATA4 regulates Fgf16 to promote heart repair after injury. Development *143*, 936.

Zhao, Y., Zhou, J., He, L., Li, Y., Yuan, J., Sun, K., Chen, X., Bao, X., Esteban, M.A., Sun, H., et al. (2019). MyoD induced enhancer RNA interacts with hnRNPL to activate target gene transcription during myogenic differentiation. Nature Communications *10*, 5787.

Zhou, L., Sun, K., Zhao, Y.U., Zhang, S., Wang, X., Li, Y., Lu, L., Chen, X., Chen, F., and Bao, X. (2015). Linc-YY1 promotes myogenic differentiation and muscle regeneration through an interaction with the transcription factor YY1. Nature Communications *6*, 1–16.